

<b>REPORT DOCUMENTATION PAGE</b>			Form Approved OMB No. 074-0188	
Public reporting burden for this collection of information is estimated to average 1 hour per response, including the time for reviewing instructions, searching existing data sources, gathering and maintaining the data needed, and completing and reviewing this collection of information. Send comments regarding this burden estimate or any other aspect of this collection of information, including suggestions for reducing this burden to Washington Headquarters Services, Directorate for Information Operations and Reports, 1215 Jefferson Davis Highway, Suite 1204, Arlington, VA 22202-4302, and to the Office of Management and Budget, Paperwork Reduction Project (0704-0188), Washington, DC 20503				
1. AGENCY USE ONLY (Leave blank)		2. REPORT DATE 6/12/1998		3. REPORT TYPE AND DATES COVERED Final: Dec. 1, 1994 – Dec. 31, 1997
4. TITLE AND SUBTITLE Phase Conjugate Injection Locking Of Laser Diode Arrays			5. FUNDING NUMBERS G: F49620-95-1-0082	
6. AUTHOR(S) Prof. Jack Feinberg			AFRL-SR-BL-TR-98- 0500	
7. PERFORMING ORGANIZATION NAME(S) AND ADDRESS(ES) University of Southern California, Dept. of Contracts and Grants University Park Los Angeles, CA 90089-1147			8. PERFORMING ORGANIZATION REPORT NUMBER	
9. SPONSORING / MONITORING AGENCY NAME(S) AND ADDRESS(ES) Air Force Office of Scientific Research/ NE Bolling AFB, Building 410 Washington, D.C. 20332-6448			10. SPONSORING / MONITORING AGENCY REPORT NUMBER	
11. SUPPLEMENTARY NOTES			19980617 033	
12a. DISTRIBUTION / AVAILABILITY STATEMENT Approved for Public Release: Distribution Unlimited			12b. DISTRIBUTION CODE	
13. ABSTRACT (Maximum 200 Words) This goal of this project is to produce a high-brightness, narrow-frequency light beam from a semiconductor laser array. We used a mutually-pumped phase conjugator to couple a single-frequency master laser into a high-power diode laser array. This injected light narrowed the frequency bandwidth of the laser array's output beam. Tuning the master laser (by adjusting its current or its temperature) then smoothly tuned the laser array, while the output beam remained diffraction limited. We compared the performance of the four types of mutually-pumped phase conjugators for injecting light into a laser array. We also invented a new technique for detecting domains hidden in photorefractive crystals. We also measured the phase of the light produced by frequency doubling in a self-phase matched optical fiber. We also measured the anisotropy of the mobility of holes in barium titanate crystals. We found that the drift mobility perpendicular to the crystal's c-axis is 40 times that along the c-axis. We also measured the calibrated small-signal gain spectrum, over a range of eight orders of magnitude, of a single-mode, flared semiconductor amplifier. We found that the detailed-balance theory of semiconductor lasers theory is not consistent with our data. We used a self-pumped phase conjugator to determine a key calibration constant in our experiments.				
14. SUBJECT TERMS semiconductor laser, phase conjugation, barium titanate			15. NUMBER OF PAGES 50	
			16. PRICE CODE	
17. SECURITY CLASSIFICATION OF REPORT UNCLASSIFIED	18. SECURITY CLASSIFICATION OF THIS PAGE UNCLASSIFIED	19. SECURITY CLASSIFICATION OF ABSTRACT UNCLASSIFIED	20. LIMITATION OF ABSTRACT UL	

## Final Report

submitted to the  
Air Force Office of Scientific Research  
Bolling AFB, Building 410,  
Washington, D.C. 20332-6448

**ATTN.: Dr. Howard Schlossberg**

- 1) Date submitted: May 12, 1998
- 2) Title: PHASE CONJUGATE INJECTION LOCKING OF LASER DIODE ARRAYS
- 3) Principal Investigator: JACK FEINBERG  
Office: (213) 740-1134, Fax: (213) 740-6653
- 4) Time period covered: DECEMBER 1, 1994 – DECEMBER 31, 1997.
- 5) Institution Name: University of Southern California, Los Angeles, CA  
90089-0484.
- 6) Federal agency identifying award number: F49620-95-1-0082.
- 7) USC identifying award number: 53-4869-5698.

# PHASE CONJUGATE INJECTION LOCKING OF LASER DIODE ARRAYS

Jack Feinberg  
Department of Physics  
University of Southern California  
Los Angeles, California 90089-0484  
(213) 740-1134

## **A) Summary of Overall Progress:**

### **FIRST YEAR:**

This goal of this project is to produce a high-brightness, narrow-frequency light beam from a semiconductor laser array. In the first project period we used a mutually-pumped phase conjugator to couple a single-frequency master laser into a high-power diode laser array. This injected light narrowed the frequency bandwidth of the laser array's output beam. Tuning the master laser (by adjusting its current or its temperature) then smoothly tuned the laser array, while the output beam remained diffraction limited. We concentrated on characterizing and optimizing the mutually-pumped phase conjugator, which is the key element for aiming light from the injecting laser into the numerous lasers making up the laser array. We compared the performance of the four types of mutually-pumped phase conjugators for injecting light into a laser array (see publication #1).

### **SECOND YEAR:**

In the second project period we pursued the main project along with a number of other, related projects. In particular, we published new results on the following:

1) A new technique for detecting domains hidden in photorefractive crystals. These  $180^\circ$  domains are usually not wanted, for they diminish the efficiency of beam-coupling in such crystals. Our simple technique maps the location of any  $180^\circ$  domains in three dimensions. (See publications 2, 3 and 4.) A 3-minute video was made (with music and captions) that used this new technique to show the motion of domains in a barium titanate crystal. (See publication #10).

2) Measurement of the phase of the light produced by frequency doubling in a self-phase matched optical fiber. (See publication #5 and # 6.)

3) Measurement of the anisotropy of the mobility of holes in barium titanate crystals. We show that the drift mobility perpendicular to the crystal's c-axis is 40 times that along the c-axis. (See publication #7)

### THIRD YEAR

In this third project period we have concentrated on generating a high-brightness light beam from a semiconductor laser array.

#### 1) Injection of array:

One method of generating a high-brightness, narrow bandwidth beam from a semiconductor laser array is to inject the array with a seeding beam from a single-mode laser. For this purpose we bought an OptoPower 10W laser bar (model OPC-A010-mmm-CS) which we had special-ordered so that its output facet was uncoated. (It normally has about a  $R=5\%$  coating.) We then AR coated this output facet to  $<1\%$ . (Coating it turned out to be nontrivial, because the array was already metalized and mounted.) We have begun experiments with the coated array using our phase-conjugate injection-locking setup. Those experiments are still in progress. We also published results using two-beam coupling to clean up the spatially distorted beam from a semiconductor array. (See publication #8).



## 2) Ring laser power converter

We continued experiments using a photorefractive ring cavity to convert a spatially distorted laser beam into a diffraction limited beam. We found a theoretically better beam-crystal geometry that decreases the Fresnel losses and increases the two-beam coupling gain. We altered the resonator geometry to ease its alignment, and then modeled the performance of the resonator vs. gain, oscillating power, output coupler reflectivity, mode size, and resonator lens strength. Our rebuilt device now includes a Faraday isolator to ensure unidirectional ring operation. Curiously, we found that our photorefractive crystal tended to depole while in the resonator. At first we thought that we had heated the crystal past its Curie temperature ( $125^{\circ}\text{C}$ ) with the laser high power circulating in the resonator, but even after taking care to dissipate the heat built up in the crystal, the crystal still depoled during resonator operation. Although this grant expired before we could obtain another crystal, we have used other funds to purchase additional  $\text{BaTiO}_3$  crystals and we are pursuing this work.

3) We measured the calibrated small-signal gain spectrum, over a range of eight orders of magnitude, of a single-mode, flared semiconductor amplifier. By measuring the amplified spontaneous emission spectrum and using a simple theory, we deduced the spontaneous emission spectrum of the amplifier. We found that the detailed-balance theory of semiconductor lasers theory is not consistent with our data. A self-pumped phase conjugator helped to determine a key calibration constant in our experiments, namely the coupling efficiency of the amplifier. This work formed part of the Ph.D. thesis of graduate student San-Ching de la Cruz, and it will be published later this year.

## Publications

- 1) S. C. de la Cruz, S. MacCormack, J. Feinberg, Q. B. He, H. K. Liu, and P. Yeh, "Effect of beam coherence on mutually pumped phase conjugators," **J. Opt. Society of America-B** 12, 1363-1369 (1995).
- 2) "Eminent Domains," an article about our work on the imaging of domains in crystals, appeared in the December 22, 1995 issue of **Science**.
- 3) V. Grubsky, S. MacCormack, and J. Feinberg, "All-optical three-dimensional mapping of 180° domains hidden in a BaTiO<sub>3</sub> crystal," **Opt. Lett.** 21, 6-8 (1996).
- 4) S. MacCormack and J. Feinberg, "Revealing 180° domains in ferroelectric crystals by photorefractive beam coupling," **Applied Optics** 35, 5961 - 5963 (1996).
- 5) V. Dominic, P. Lambelet, and J. Feinberg, "Measurement of the phase of second-harmonic generation in SK5 glass," **Opt. Lett.** 20, 444-446 (1995).
- 6) P. Lambelet and J. Feinberg, "Phase of second-harmonic light self-generated in a glass fiber," **Opt. Lett.** 21, 925-927 (1996).
- 7) D. Mahgerefteh, D. Kirillov, R. S. Cudney, G. D. Bacher, R. M. Pierce, and J. Feinberg, "Anisotropy of the hole drift mobility in barium titanate," **Phys. Rev. B** 53, 7094 - 7098 (1996).
- 8) S. MacCormack, G. D. Bacher, J. Feinberg, S. O'Brien, R. J. Lang, M. B. Klein, B. A. Wechsler, "Powerful, diffraction-limited semiconductor laser using photorefractive beam coupling," **Opt. Lett.** 22, 1-3 (1997).
- 9) J. Feinberg and A. Rebane, "Ballistic light imaging with temporal holography: Using causality to see through a scattering medium," in *Imaging Brain Structure and Function* edited by Lester, Felder and Lewis, Annals of the New York Academy of Sciences, Volume 82, 272-285 (1997).
- 10) "Dancing Domains," a 3-minute VHS video (Marmot Productions, 1996).

## Interactions

### Conferences, etc.

Contributed talk, "Dynamic mapping of 180° domains hidden in a photorefractive crystals," V. Grubsky, S. MacCormack, and J. Feinberg, Conference on Lasers and Electrooptics (CLEO), Anaheim, California, June 2-7, 1996.

Invited Talk, "Photorefractive Materials," Institute of Physics Technical Meeting on Nonlinear Optical Materials, Defense Research Agency, Malvern, Great Britain, April 17, 1996.

Contributed talk, "Frequency locking of two elements of a laser diode array using mutually pumped phase conjugation," S.-C. De La Cruz, S. MacCormack, P. Lambelet and J. Feinberg, Photorefractive Materials, Effects and Devices, Estes Park, Colorado, June 11-14, 1995.

Contributed talk, "Yet another explanation for why a Cat-conjugator can emit a frequency-shifted beam", D. Noraev, P. Lambelet, and J. Feinberg, Photorefractive Materials, Effects and Devices, Estes Park, Colorado, June 11-14, 1995.

Contributed talk, "The Swiss cheese effect," S. MacCormack and J. Feinberg, Photorefractive Materials, Effects and Devices, Estes Park, Colorado, June 11-14, 1995.

Invited talk, "Seeing Through Chickens," W.V.T. Rusch Honors Program, USC, Feb. 10, 1995.

Invited talk, "Seeing Through Chickens," Loyola Marymount University, Feb. 10, 1995.

### Collaborations with

(1) Q. Byron He and (2) Hua-Kuang Liu  
Jet Propulsion Laboratory,  
California Institute of Technology,  
and

(3) Prof. Pochi Yeh  
Department of Electrical and Computer Engineering,  
University of California at Santa Barbara.

(4) Prof. Robert Eason  
Optoelectronics Research Centre  
University of Southampton

Southampton, England

(5) Patrick Lambelet  
Laboratoire d'Optique Appliquée  
Ecole Polytechnique Fédérale  
Lausanne, Switzerland

(6) Marvin Klein and (7) Barry Wechsler  
Hughes Research Labs  
Malibu, CA

(8) Steve O'Brien and (9) Robert Lang  
SDL, Inc.  
Santa Clara, CA

(10) Professor Roger Cudney  
C.P. 22800  
Ensenada, Baja California Norte,  
Mexico

(11) Professor Harold Fetterman  
UCLA  
Los Angeles, CA

### **Honors or Awards**

The principal investigator, Jack Feinberg, won the 1995 Discover Award for "Technological Innovation In The Field Of Sight." This was a national competition. An article about my work was printed in the June, 1995 issue of Discover magazine.

### **Personnel Supported**

Jack Feinberg, Principal Investigator  
San-Ching de la Cruz, Graduate Student  
Stuart MacCormack, Research Associate  
Martin Loebel, Visiting Scientist  
Dmitry Starodubov, Research Scientist

### **New Discoveries, Inventions, or Patent Disclosures**

A new method for detecting and mapping 180° domains hidden in photorefractive crystals. No patent disclosure filed.

# Effect of beam coherence on mutually pumped phase conjugators

San-Ching De La Cruz, Stuart MacCormack, and Jack Feinberg

*Departments of Physics and Electrical Engineering,  
University of Southern California, Los Angeles, California 90089-0484*

Q. Byron He\* and Hua-Kuang Liu

*Jet Propulsion Laboratory, California Institute of Technology,  
4800 Oak Grove Drive, Pasadena, California 91109*

Pochi Yeh

*Department of Electrical and Computer Engineering,  
University of California, Santa Barbara, Santa Barbara, California 93106*

The performance of four different mutually pumped phase conjugators in barium titanate depends on the mutual coherence of the two input beams. In three of the conjugators the use of fully mutually coherent input beams enhances the overall phase-conjugate reflectivity. We find that backscattering and transmission gratings in the photorefractive crystal both contribute to the phase-conjugate signal and that their relative strength depends on the relative coherence of the two input beams. We numerically solve coupled-wave equations that include all gratings and find reasonable agreement between our theory and our experimental data.

## 1. INTRODUCTION

Imagine trying to inject light into the gain regions of a present-day laser-diode array. Such a laser-diode array might measure 1 cm across, but its 20 or so gain regions are each only  $200\text{ }\mu\text{m}$  across  $\times 1\text{ }\mu\text{m}$  high. Injecting light precisely into these lasing regions is like trying to thread 20 needles in a haystack simultaneously. However, if the output from the laser array is sent into a photorefractive crystal, and if a separate light beam is also directed into the same crystal, then the crystal could, in principle, connect the two light beams, sending each beam back down the path of the other. Acting as a mutually pumped phase conjugator, the crystal would transform each light beam into the phase-conjugate replica of the other light beam. In the above application the crystal would direct the injected light beam precisely into the lasing regions of the array. The two incident light beams need not be coherent with each other, although they should have the same nominal wavelength.

Using the double phase-conjugate mirror (DPCM),<sup>1</sup> a number of authors have demonstrated short-lived injection locking of a laser.<sup>2,3</sup> MacCormack *et al.*<sup>4</sup> used a bird-wing<sup>5</sup> conjugator and obtained stable locking between two laser diodes.

When two lasers are connected by a phase conjugator and the lasers become phase locked, their light beams become mutually coherent. Can the crystal continue to act as a mutually pumped phase conjugator with mutually coherent light beams? We show below that the answer depends on the particular geometry of the mutually pumped phase conjugator.

First we give a heuristic explanation of how mutually pumped phase conjugators work.<sup>5,6</sup> Let the two input beams be labeled 2 and 4. (We use this counterintuitive beam-numbering scheme to stick to the convention of Ref. 7.) Light randomly scattered from beam 2 travels across beam 2 and writes a multitude of different beam-fanning gratings. Beam 4 tends to erase most of these gratings. However, beam 4 will be incident at the Bragg angle for some small set of these fanning gratings, and it will efficiently deflect from them. The deflected beam 4 interferes with the incident beam 4 to reinforce selectively only the deflecting gratings. Simultaneously the same process occurs with beams 2 and 4 switched. The result is that the shared fanning gratings grow in strength, whereas the unshared fanning gratings collapse. The shared fanning gratings make up a volume hologram that converts beam 2 into the phase-conjugate replica of beam 4, and vice versa. The above description applies to the DPCM. The bridge,<sup>8</sup> the bird-wing, and the British (also known as the mutual incoherent beam coupler)<sup>9</sup> conjugators, all shown in Fig. 1, are somewhat more complicated; they have more than one interaction region, and in the latter two devices the light beams are also internally reflected at one or more crystal faces.

Let the two input beams have wave vectors  $\mathbf{k}_2$  and  $\mathbf{k}_4$ , respectively. If these two beams are at least partially coherent with each other, then they will create gratings in addition to the shared transmission grating described above. These additional gratings affect the performance of the conjugator. Figure 2 shows that input beam 2 can write a backscattering grating, with wave vector  $\mathbf{k} = 2\mathbf{k}_2$ , with the counterpropagating conjugate beam that comes

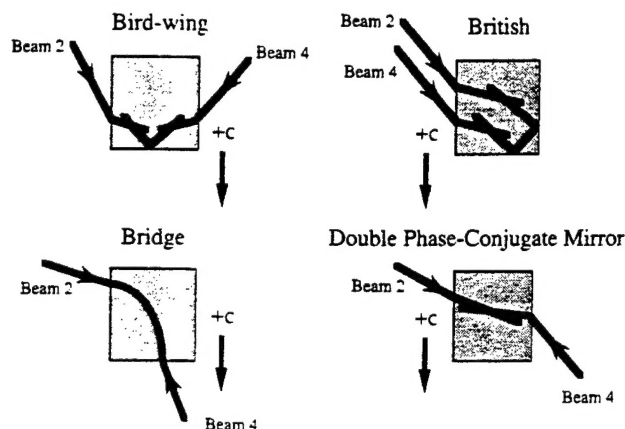


Fig. 1. Four different mutually pumped phase conjugators. The British and the bird-wing conjugators use internal reflections to guide the beams.

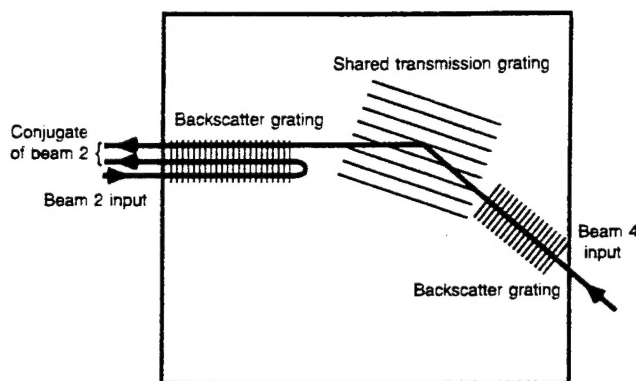


Fig. 2. Two contributions to the phase-conjugate signal: the shared transmission grating deflects each input beam into the conjugate of the other beam, whereas the backscattering gratings deflect each input beam into its own phase conjugate. Backscattering gratings form only if the two input beams are at least partially mutually coherent.

from beam 4. Similarly, along the path of beam 4 will be a backscattering grating with wave vector  $\mathbf{k} = 2\mathbf{k}_4$ . We note that if the input beams are mutually coherent they will also write a reflection grating of wave vector  $\mathbf{k} = \mathbf{k}_2 - \mathbf{k}_4$ . This reflection grating contributes only weakly and indirectly to the phase-conjugate signal, and its principal effect is to deflect a portion of the input beams out of the interaction region.

In general there are two primary contributions to the phase-conjugate signal: (1) the beam deflected from the shared transmission grating and (2) the beam reflected from backscattering gratings. The strength of only the backscattering gratings depends on the degree of mutual coherence between the input beams. In this paper we measure how these two contributions to the phase-conjugate signal vary as we alter the mutual coherence of the two incident light beams. Our measurement techniques are similar to those employed by Gruneisen *et al.*, who measured the total phase-conjugate signal in the DPCM.<sup>10</sup> We also present theoretical fits to our data, using a recently developed theory of four-wave mixing of partially coherent beams in such conjugators.<sup>11</sup>

## 2. EXPERIMENT

We operated our argon-ion laser at  $\lambda = 514.5$  nm with an étalon to increase its coherence length to a few me-

ters. A beam splitter (shown in Fig. 3) generated the two extraordinary-polarized input beams. We matched the optical paths of the two beams from the laser to the conjugator to within 10 cm. We equalized the beam powers incident at the entrance to the conjugator with a half-wave plate and polarizer. For all our measurements the input beam powers were typically  $\sim 14$  mW/beam. At the conjugator the beams' diameters ( $1/e$  intensity) were 0.75 mm. We monitored the input beam power and the phase-conjugate signal for both input beams, using reflections from uncoated optical wedges. We positioned an aperture in front of each detector to ensure that we measured only the phase-conjugate beam. A Faraday isolator reduced any feedback into the argon-ion laser by at least 30 dB.

We used nominally undoped photorefractive crystals of  $\text{BaTiO}_3$  to form the different conjugators. Unable to find one  $\text{BaTiO}_3$  crystal that could support all four conjugators, we used two crystals that exhibited good beam fanning: a crystal named Hua [6.05 mm  $\times$  4.58 mm  $\times$  5.89 mm (parallel to the  $c$  axis)], for the bridge and the bird-wing conjugators, and a crystal named Twin [5.39 mm  $\times$  5.19 mm  $\times$  5.40 mm ( $c$  axis)] for the DPCM and the British conjugators.

We controlled the mutual coherence of the two input beams as follows. We placed a piezoelectric transducer up against a mirror mount to give beam 4 a controllable-amplitude, triangle-wave phase jitter. We set the jitter frequency at 870 Hz to take advantage of a mechanical resonance in the mirror mount. The resulting phase jitter caused any optical interference pattern written between the two input beams to oscillate spatially at 870 Hz. This frequency was an order of magnitude faster than the measured response rate of our crystals at the optical intensities used in our experiment, so the crystal effectively time averaged the phase jitter and thereby reduced the effective mutual coherence of the two input beams. Changing the amplitude of the voltage on the piezoelectric transducer varied the mutual coherence of the two input beams. We observed that imparting a phase jitter to an input beam had no effect on that beam's fanning in the crystal. This result was expected because in beam

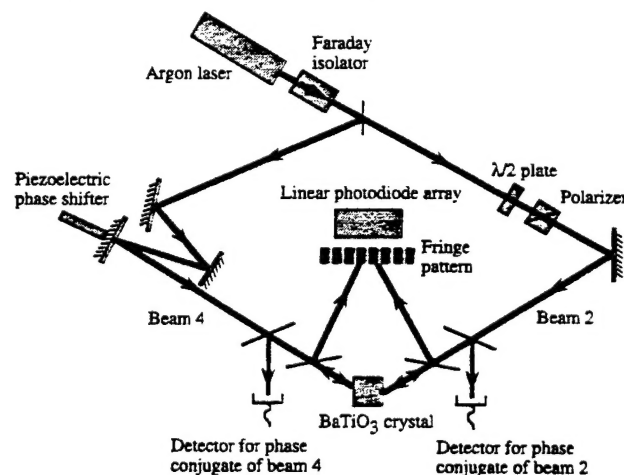


Fig. 3. Experimental setup. The piezoelectric pusher imparts a phase jitter to cause input beams 2 and 4 to be partially mutually incoherent, as measured by the linear photodiode array. The half-wave plate and the polarizer form a variable attenuator to equalize the powers of the two input beams at the crystal.



fanning all the rays originate from the same beam, so the same phase jitter was present on all these rays and canceled out.

We measured the effective mutual coherence of the two input beams by interfering them and measuring their fringe visibility  $\nu \equiv (I_{\max} - I_{\min}) / (I_{\max} + I_{\min})$ . This fringe visibility ranges from  $\nu = 0$  with mutually incoherent input beams to  $\nu = 1$  with fully mutually coherent input beams. We monitored the interference fringes generated by overlapping equal intensities of both input beams on a 512-element linear photodiode array whose 20-ms readout time was comparable with the crystal's response time. We determined  $\nu$  by dividing the output from the linear photodiode array by the output produced with mutually incoherent beams ( $\nu = 0$ ) and fitting the resulting curve to a sine wave to determine its visibility, as shown in Fig. 4. We could vary the fringe visibility over almost its full range, from  $\nu = 0.05$  to  $\nu = 0.95$ .

We initially set up four different mutually pumped conjugators, using mutually incoherent beams at angles similar to those described in Refs. 1, 5, 8, and 9. We then adjusted the beam angles and positions to optimize the stability and the power reflectivity of the phase-conjugate signals for both beams.

Starting from fully incoherent beams, we decreased the voltage applied to the piezoelectric transducer, measured the corresponding fringe visibility, and then allowed the conjugator to stabilize and to adapt to the change in mutual coherence. At each coherence point we measured six quantities:

- (i) the total cw phase-conjugate reflectivity of beam 2;
- (ii) the total cw phase-conjugate reflectivity of beam 4;
- (iii) the phase-conjugate transmission of beam 4 (we blocked beam 2 and within a few milliseconds measured any signal that was phase conjugate to beam 2; this was a measure of the fraction of beam 4 converted into the phase conjugate of beam 2 because the shutter momentarily blocked any contribution to the phase-conjugate signal from the backscattering of beam 2);
- (iv) the phase-conjugate transmission of beam 2, detected similarly to the measurement of (iii) above;
- (v) the purely backscattered contribution to the phase conjugate of beam 2 (we momentarily blocked beam 4 and measured any signal that was phase conjugate to beam 2);
- (vi) the purely backscattered contribution to the phase conjugate of beam 4, detected similarly to the measurement of (v) above.

We usually found no difference if we approached a particular value of  $\nu$  from below or above; however, for a small number of cases (not shown in Figs. 5–9 below), we observed bistable operation, with the extreme case that some conjugators would not self-start with fully coherent input beams.

When using fully coherent input beams, we found that tapping one of the beam-steering mirrors caused the phase-conjugate signal either to drop immediately from a maximum value or to increase from a minimum value, but never to oscillate about an intermediate value. This effect implies that the phase shift between the transmitted and the backscattered beams was always  $0^\circ$  or  $180^\circ$ , as expected for a backscattering grating in  $\text{BaTiO}_3$

with purely diffusive charge transport and no applied dc electric field.<sup>12</sup>

Figures 5–9 show the dependence of both the total phase-conjugate reflectivity and the transmission on the mutual coherence of the two input beams. Both quantities are the ratio of powers, with no corrections for Fresnel loss. The reflectivity data include both the transmitted and the backscattered contributions to the conjugate signals, whereas the transmission data reveal only the transmitted signal. The solid curves are fits to the total reflectivity, as detailed in Section 3. The phase-conjugate reflectivities and transmissions of the different conjugators depended on the particular angles and alignment of the two incident beams. Our data show behavior typical for each geometry, given that we optimized the reflectivity of the conjugators.

With mutually coherent input beams the stability of the conjugate signals depended critically on the stability of the setup, and we eventually used smaller and more stable 38.1-cm-high pedestal mounts to reduce fluctuations greatly.<sup>13</sup> Such reduced fluctuations can be seen by comparison of the British I and the British II conjugators shown in Figs. 8 and 9, respectively. These fluctuations are likely caused by small drifts external to the crystal. If the reflectivity fluctuated (usually on a time scale of seconds), we plotted its maximum value, and we represent these fluctuations by vertical bars on a few data points. The horizontal error bars represent the uncertainty in the relative coherence values. This uncertainty was most noticeable at the higher coherence values, where slight air currents and vibrations became

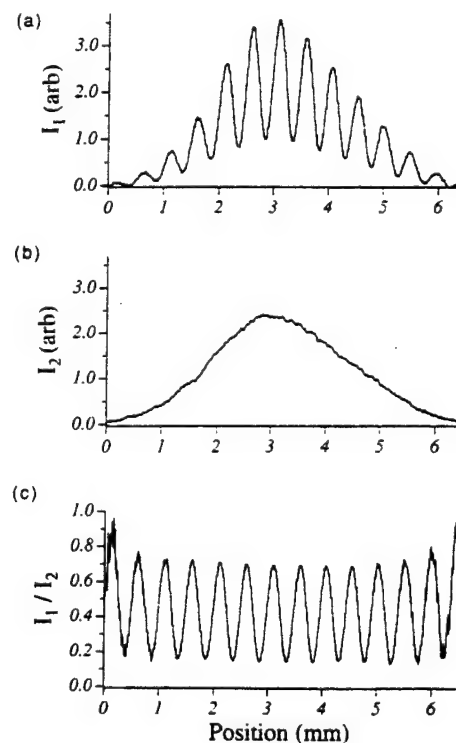


Fig. 4. Measurement of the mutual coherence  $\nu$  of the two input beams. (a) Interference fringes produced by two partially mutually coherent beams with a background offset subtracted. (b) No fringes produced by two completely incoherent beams, with the same offset subtracted. Division of trace (a) by trace (b) produces the sinusoidal fringe pattern (c), which in this case has a measured visibility  $\nu = 0.54$ .

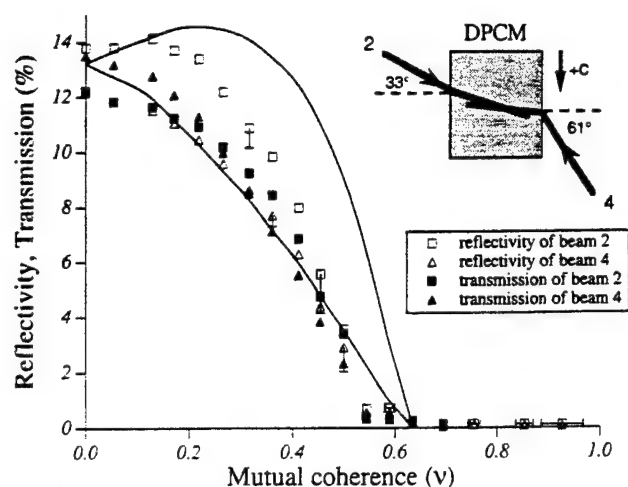


Fig. 5. Behavior of the DPCM mutually pumped phase conjugator as we alter the mutual coherence of the input beams from mutually incoherent ( $v = 0$ ) to mutually coherent ( $v = 1$ ). The reflectivity data include contributions from both transmission and backscattering gratings, whereas the transmission data come only from the transmission grating. The solid curves are our theoretical fits to the two total reflectivities. The horizontal and the vertical bars on a few representative data points show the uncertainty in the measured coherence values and the fluctuations in the measured signals. Note that the DPCM conjugator turns off when the input beams become too coherent with each other.

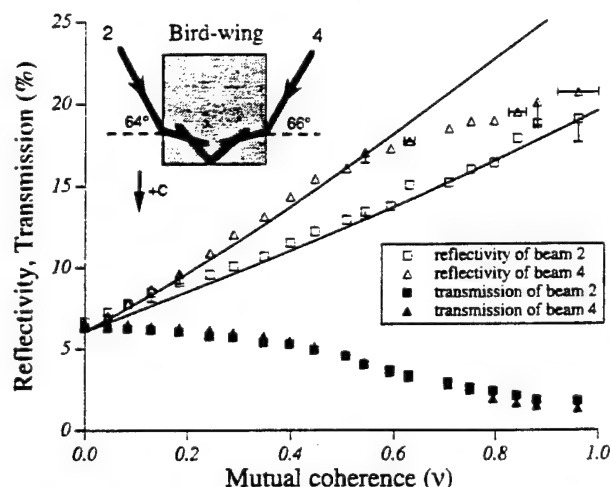


Fig. 6. Bird-wing conjugator. The symmetry of the beam paths inside the crystal ensures similar data for the two input beams. The fits are to the reflectivity data.

important and limited the fringe visibility  $v < 0.95$ . All the phase-conjugate signals were stable, with mutually incoherent input beams. Table 1 lists our subjective comparison of all four conjugators.

The British conjugator exhibited different behaviors according to the position and the angle of the input beams. Figure 8 shows data for British I, in which we positioned both input beams close to the  $+c$  face of the crystal. The resulting coupling channel was short, and the curvature of the two input beams had a pronounced asymmetry inside the crystal, with beam 2 fanning more strongly than beam 4. In contrast, Fig. 9 shows data for British II, in which we positioned both input beams slightly further from the  $+c$  face and at smaller angles of incidence. This conjugator developed a longer coupling channel, with both beams now having similar curvatures inside the crystal.

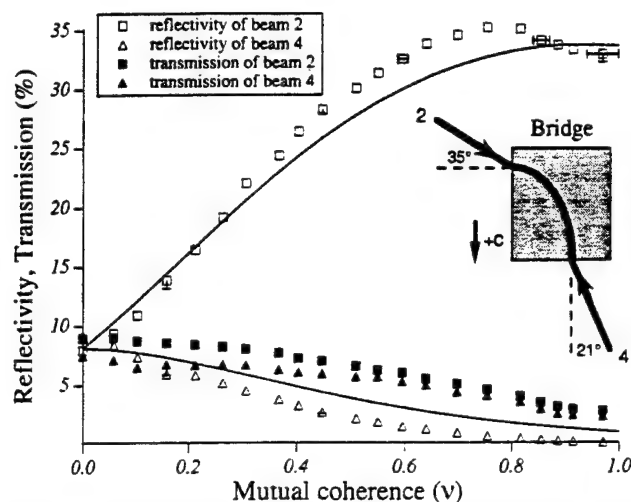


Fig. 7. Bridge conjugator. The asymmetry shown in the reflectivities of the bridge conjugator is caused by the difference in the sign of the backscattering coupling strength for the two input beams. The fits are to the reflectivity data.

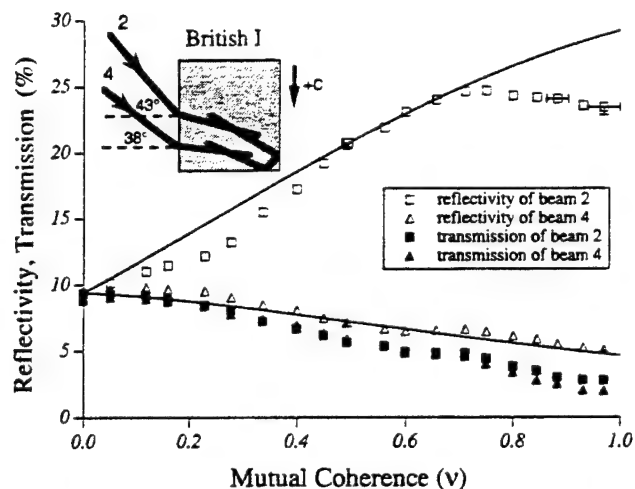


Fig. 8. British I conjugator has a small loop in the crystal. The fits are to the reflectivity data.

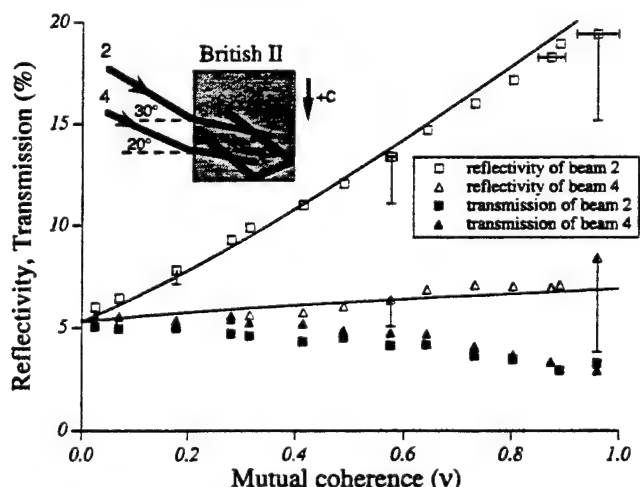


Fig. 9. British II conjugator has a larger loop in the crystal. The large signal fluctuations shown in these data were caused by a less stable optical setup. When we switched to a more stable setup the British conjugator was the least noisy of the four types of conjugator investigated. The fits are to the reflectivity data.



**Table 1. Ease-of-Use and Signal Fluctuations of the Mutually Pumped Phase Conjugators**

Conjugator	Ease of Setup	Signal Fluctuations
DPCM	Easy	Moderate
Bird wing	Somewhat easy	Small
Bridge	Somewhat difficult	Small
British	Difficult	Very small

In general, as we increased the mutual coherence of the two input beams at least one conjugate signal increased, whereas both transmissions decreased. The exception was the DPCM shown in Fig. 5, which usually ceased to operate when the input beams became coherent with each other ( $\nu = 1$ ). We could obtain phase-conjugate signals from the DPCM with fully coherent input beams, but only after tedious alignment. Both phase-conjugate outputs in the bird-wing conjugator and the British II conjugator increased as  $\nu \rightarrow 1$ , whereas in the bridge and the British I conjugators one conjugate signal grew, but the other diminished in power. At  $\nu \sim 1$ , we checked that the bridge, the bird-wing, and the British conjugators were not acting as self-pumped conjugators by confirming that both input beams were required for sustained conjugation.

In the DPCM we occasionally observed that the phase-conjugate reflectivity of beam 2 increased steadily as  $\nu$  increased from 0 to 0.25, where the reflectivity then dropped abruptly, as predicted by our theoretical plots. However, most of the time the reflectivity of beam 2 in the DPCM began to collapse at  $\nu \approx 0.1$ , as shown in Fig. 5. The DPCM data presented here agree in general with those reported by Gruneisen *et al.*,<sup>10</sup> with the exception that their DPCM conjugated weakly even with high mutual coherence. We note that our theory does not take into account the effects of conical scattering, which can cause significant loss.<sup>14</sup> Also, unequal fanning losses experienced by beams 2 and 4 can cause the different reflectivities observed for the two beams at  $\nu = 0$ .

As the mutual coherence of the two input beams is increased, backscattering gratings increase in strength and affect the performance of the conjugators in three ways. First, each input beam can now exchange energy with its own phase-conjugate beam through two-beam coupling, with the direction of energy transfer being determined by the orientation of the beams with respect to the crystal's  $c$  axis. Second, this two-beam coupling can create an imbalance in the two input beams' intensities inside the crystal; this imbalance reduces the cross-erasure efficiency, which weakens the transmission grating. Third, backscattering gratings can decrease the overall transmission of a conjugator by simply reflecting energy away from the transmitted phase-conjugate beam.

Figure 10 shows how the computed amplitude coupling coefficient  $\gamma_b$  of a backscattering grating varies as a function of the angle  $\theta$  between the beams' propagation directions inside the crystal and the  $c$  axis.<sup>15</sup> For this calculation we use recent values for the effective Pockels coefficients, which include the small influence of elastic stiffness, piezoelectric stress, and the elasto-optic effect.<sup>16</sup> We find that input beams traveling at angles  $6^\circ < \theta < 90^\circ$  are depleted by backscattering gratings. We estimate that, in the bird-wing and the British conjugators,

the angles of both conjugate beams with respect to the  $c$  axis lie in the range  $95^\circ < \theta < 150^\circ$ , so, according to Fig. 10, in these conjugators both conjugate beams gain from backscattering gratings at the expense of the input beams. To estimate the contribution of backscattering gratings to the phase-conjugate signal we use the relation

backscatter reflectivity

$$= (\sqrt{\text{total reflectivity}} \pm \sqrt{\text{transmission}})^2,$$

where the terms are added if the components are out of phase or are subtracted if they are in phase, and we neglect the contribution of reflection grating to the conjugate signal. For example, for the bridge conjugator the computed backscattering power reflectivity for beam 2 with fully mutually coherent beams ( $\nu = 1$ ) is  $(\sqrt{33\%} - \sqrt{2.4\%})^2 = 17.6\%$ . This result agrees with our measured backscattered power reflectivity of 18%. We performed such calculations for all the data shown and found good agreement between the calculated and the measured backscattered contributions. This finding confirms that the conjugate signals are due to transmission and backscattering gratings and that reflection gratings can be neglected in the analysis of these experiments.

Backscattering gratings affect the different conjugators differently. The effect of backscattering gratings is seen most clearly in the data of Fig. 7 for the bridge conjugator. Here one conjugate beam travels somewhat opposite the  $c$  axis at  $\theta \sim 130^\circ$  and so gains from its backscattering grating, whereas the other conjugate beam is at  $\theta \sim 70^\circ$  and so is depleted by its backscattering grating. This effect causes the asymmetry seen in the reflectivity data. In contrast, in the bird-wing conjugator the path of the two beams are symmetric about the  $c$  axis, and both conjugate beams gain equally by backscattering. Figure 6 confirms that making the input beams coherent has little effect on the transmission grating, inasmuch as the strength of this grating depends only on the rela-

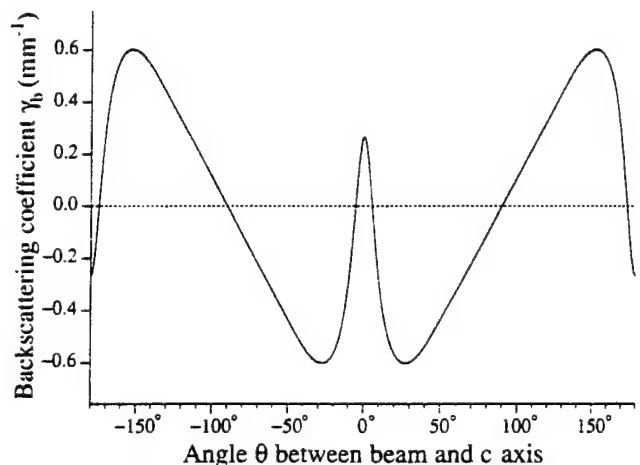


Fig. 10. Amplitude two-beam coupling efficient  $\gamma_b$  for a beam and its counterpropagating beam as a function of the internal angle between the beam and the BaTiO<sub>3</sub> crystal's  $c$  axis. A positive coupling coefficient means that the beam is gaining energy from its counterpropagating beam. For example, a beam propagating between  $6.7^\circ$  and  $90^\circ$  to the  $+c$  axis is depleted by its counterpropagating beam. This calculation uses recent values for the electro-optic coefficients<sup>12</sup> and assumes an effective charge-carrier density of  $N = 5 \times 10^{16} \text{ cm}^{-3}$  and  $e$ -polarized rays at  $\lambda = 514.5 \text{ nm}$ .

tive intensity of the two input beams and not on their mutual coherence. For the DPCM, as the input beams are made more coherent with each other, the resulting backscattering gratings amplify input beam 4 and deplete input beam 2, and the resulting intensity imbalance so weakens the primary transmission grating that it collapses, as shown in Fig. 5. We confirmed this effect by increasing the power of input beam 2 in the DPCM while keeping the power of beam 4 constant. We found that conjugation would then persist even with fully coherent beams because now the intensities of the input beams were more closely matched inside the crystal. In contrast, conjugation ceased when we decreased the power of beam 2. Evidently the bridge and the British conjugators fall somewhere between the bird wing and the DPCM. These conjugators experience an intensity imbalance with mutually coherent input beams, but not enough to cause the transmission grating to collapse.

### 3. THEORY

We write coupled-wave equations that include transmission, reflection, and backscattering gratings,<sup>7</sup> and we also include the mutual coherence parameter  $\beta_{ij}$  between beams  $i$  and  $j$ .<sup>17</sup> For a single interaction region we obtain

$$\begin{aligned}\frac{dA_1}{dz} &= \gamma_t \frac{A_1 A_4^* + A_2^* A_3}{I_0} A_4 \\ &+ \gamma_r \frac{|\beta_{13}| A_1 A_3^* + |\beta_{24}| A_2^* A_4}{I_0} A_3 \\ &+ \gamma_b \frac{|\beta_{12}| A_1 A_2^*}{I_0} A_2 - \alpha A_1, \\ \frac{dA_2^*}{dz} &= \gamma_t \frac{A_1 A_4^* + A_2^* A_3}{I_0} A_3^* \\ &+ \gamma_r \frac{|\beta_{13}| A_1 A_3^* + |\beta_{24}| A_2^* A_4}{I_0} A_4^* \\ &+ \gamma_b \frac{|\beta_{12}| A_1 A_2^*}{I_0} A_1^* + \alpha A_2^*, \\ \frac{dA_3}{dz} &= \gamma_t \frac{A_1 A_4^* + A_2^* A_3}{I_0} A_2 \\ &+ \gamma_r \frac{|\beta_{13}| A_1^* A_3 + |\beta_{24}| A_2 A_4^*}{I_0} A_1 \\ &- \gamma_b \frac{|\beta_{34}| A_3 A_4^*}{I_0} A_4 + \alpha A_3, \\ \frac{dA_4^*}{dz} &= -\gamma_t \frac{A_1 A_4^* + A_2^* A_3}{I_0} A_1^* \\ &+ \gamma_r \frac{|\beta_{13}| A_1^* A_3 + |\beta_{24}| A_2 A_4^*}{I_0} A_2^* \\ &- \gamma_b \frac{|\beta_{34}| A_3 A_4^*}{I_0} A_3 - \alpha A_4^*.\end{aligned}$$

The boundary conditions are

$$A_1(0) = A_3(L) = 0,$$

$$\frac{|A_4(0)|^2}{|A_2(L)|^2} = q,$$

where  $A_2$  and  $A_4$  are amplitudes of the input beams and

$A_1$  and  $A_3$  are their respective conjugates;  $I_0 = |A_1|^2 + |A_2|^2 + |A_3|^2 + |A_4|^2$  is the total intensity; and  $\gamma_t$ ,  $\gamma_r$ ,  $\gamma_b$ ,  $\gamma_b'$  are the coupling coefficients for the transmission, the reflection, and the two backscattering gratings, respectively. The backscattering gratings for the two input beams can have different strengths in general.  $L$  is the interaction length, and  $z$  is the direction of propagation for beams 1 and 4. Also,  $\alpha$  is the bulk absorption coefficient, and  $q$  is the power ratio of the two incident input pump beams just inside their respective crystal faces. When the two input beams are mutually incoherent, i.e., when  $|\beta_{24}| = |\beta_{13}| = |\beta_{12}| = |\beta_{34}| = 0$ , the coupled-wave equations reduce to the conventional equations, where only the transmission grating is present.<sup>6</sup> Because the photorefractive effect in BaTiO<sub>3</sub> crystals is dominated by diffusive charge transport, here the coupling coefficients are all real numbers. We simplify the coupled equations by approximating  $|\beta_{24}| = |\beta_{13}| = |\beta_{12}| = |\beta_{34}| = |\beta|$  because we calculate that under experimental conditions the differences between the  $|\beta_{ij}|$  values are less than ~5%. Although our theory is based on a one-interaction-region model, the equations can be extended to multiple regions with different coupling strengths.<sup>18</sup>

We solve the coupled-wave equations with standard fourth-order Runge-Kutta and shooting algorithms. The mutual coherence is equal to the measured fringe visibility,  $|\beta| = \nu$ , because the two beams that we interfere in our visibility measurements had equal intensity.<sup>17</sup> We use our measured values for the bulk absorption of the BaTiO<sub>3</sub> crystal ( $\alpha = 2.6 \text{ cm}^{-1}$  in Hua and  $\alpha = 1.5 \text{ cm}^{-1}$  in Twin). For each conjugator we calculate the ratio  $q$  of the input beam powers just inside the entrance face of the crystal from our measured incident beam power and the measured Fresnel loss at the crystal surface.

We fit our experimental data with four coupling-strength parameters ( $\gamma_t \cdot L$ ,  $\gamma_r \cdot L$ ,  $\gamma_b \cdot L$ ,  $\gamma_b' \cdot L$ ). We first choose  $\gamma_t \cdot L$  to make the computed reflectivities match the experimental values measured with mutually incoherent beams ( $\nu = 0$ ). We then adjust the values of the remaining parameters to best fit the measured phase-conjugate reflectivities with  $\nu \neq 0$ , as shown by the solid curves in Figs. 5–9. For DPCM, where the input beams are nearly counterpropagating, we impose the additional restriction  $\gamma_b = -\gamma_b'$ . Table 2 shows that the resulting gain-length products are well within the range expected for BaTiO<sub>3</sub> and have the correct sign for the given beam directions in the crystal. For example, from the measured angles of incidence of the input beams and the calculated backscattering coefficient of Fig. 10

Table 2. Values of the Fitting Parameters<sup>a</sup>

Conjugator	$\gamma_t \cdot L$	$\gamma_r \cdot L$	$\gamma_b \cdot L$	$\gamma_b' \cdot L$	$\alpha \cdot L$	$L$ (mm)
DPCM	2.8	2.2	1.1	-1.1	0.5	6.0
Bridge	2.9	1.0	4.1	-0.4	0.65	4.5
Bird wing	3.3	0.5	2.3	2.4	0.9	8.0
British I	3.9	0.7	2.4	1.2	1.1	11.0
British II	3.3	1.1	2.1	0.6	0.76	11.5

<sup>a</sup>Amplitude gain times length for the transmission, the reflection, the two backscattering gratings, and the intensity absorption used in our theoretical fits. A negative value for the backscattering coefficient corresponds to a depletion of the conjugate signal. Although not required for the fits, our estimate of the interaction length ( $\pm 1$  mm) inside each crystal, obtained by observation of the actual beam paths, is also provided.

we expect that, in the DPCM and in the bridge conjugator, backscattering gratings will decrease the conjugate of beam 4, and not of beam 2. In these two conjugators the phase-conjugate to beam 4 travels at angles  $6^\circ < \theta < 90^\circ$  with respect to the positive  $c$  axis, which makes  $\gamma_b < 0$ . For all other cases  $\gamma_b > 0$  and  $\gamma_{b'} > 0$ , and the backscattering gratings couple energy from each input beam into its respective phase-conjugate beam. We noticed that increasing the value of  $\gamma_r$  always decreases the strength of the conjugate signal for all four conjugators.

#### 4. CONCLUSION

With two mutually incoherent light beams incident upon a mutually pumped phase conjugator, each phase-conjugate signal comes exclusively from the other light source. However, when the two incident light beams are mutually coherent, each phase-conjugate signal is made up of a mixture of the light from both light sources. From the viewpoint of locking lasers with such conjugators, both the transmitted and the backscattered components are useful for injection locking because both are at the same frequency and are phase conjugate to the output of the slave laser. However, because the backscattering grating cannot respond to any light modulations faster than the grating's response time, only the transmitted component can phase lock or phase modulate a laser.

Of the four mutually pumped phase conjugators investigated here, only the bird-wing and the British conjugators provide two conjugate output beams when the two input beams are fully mutually coherent. The bridge conjugator produces only one output beam of significant intensity when the beams are coherent. This result might be advantageous in laser-locking schemes in which feedback into the injecting laser is undesirable. The DPCM ceases operation with fully mutually coherent beams. A one-region, one-dimensional numerical model was able to fit the main trends of our data with reasonable values for all the fitting parameters.

#### ACKNOWLEDGMENTS

Research at the University of Southern California was supported by U.S. Air Force Office of Scientific Research grant F49620-92-J-0022.

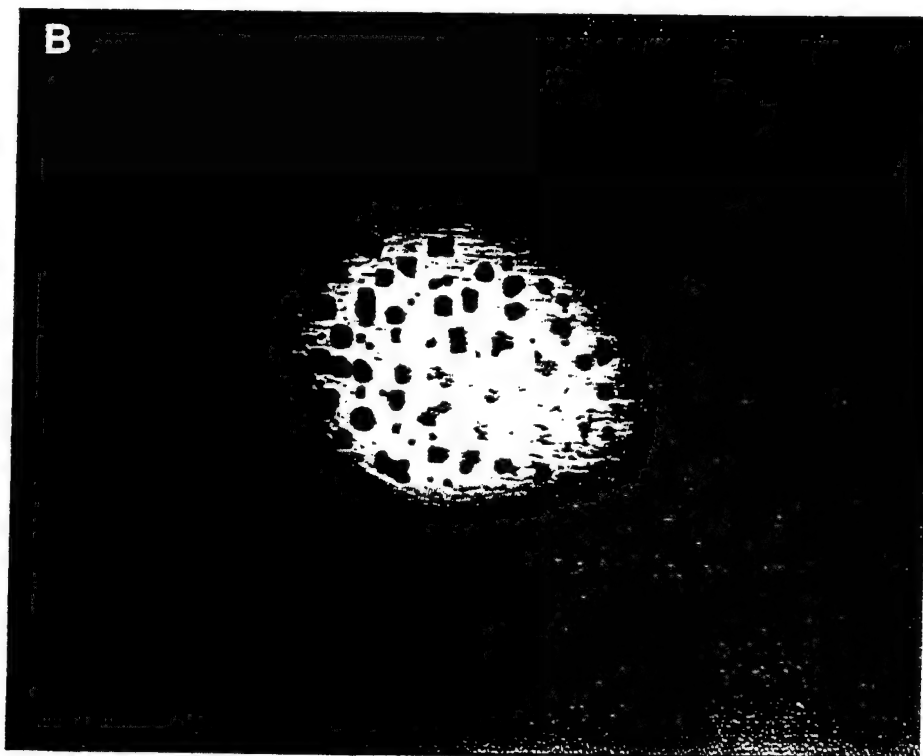
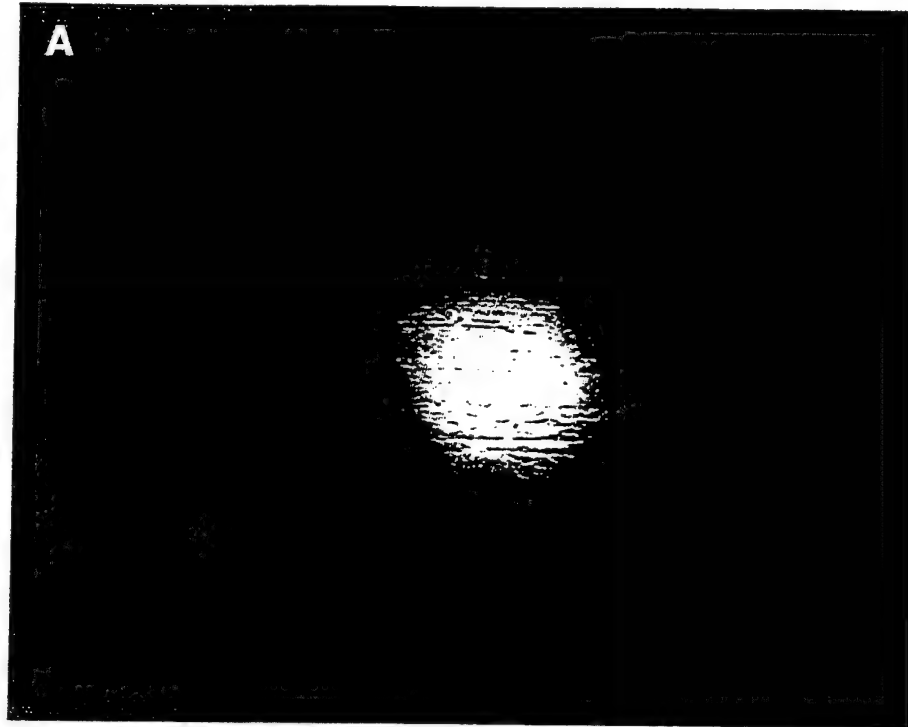
\*Present address, Energy Power Group, 900 South Shackleford Road, Little Rock, Arizona 72211.

#### REFERENCES AND NOTES

1. S. Weiss, S. Sternklar, and B. Fischer, "Double phase-conjugate mirror: analysis, demonstration, and applications," *Opt. Lett.* **12**, 114 (1987). Note that the orientation of the  $c$  axis of our DPCM differs from that shown in Fig. 1 of this reference.
2. S. Sternklar, S. Weiss, M. Segev, and B. Fischer, "Beam coupling and locking of lasers using photorefractive four-wave mixing," *Opt. Lett.* **11**, 528 (1986).
3. M. W. Wright and J. G. McInerney, "Injection locking semiconductor lasers with phase conjugate feedback," *Opt. Commun.* **110**, 689 (1994).
4. S. MacCormack, J. Feinberg, and M. H. Garrett, "Injection locking a laser-diode array with a phase-conjugate beam," *Opt. Lett.* **19**, 120 (1994).
5. M. D. Ewbank, "Mechanism for photorefractive phase conjugation using incoherent beams," *Opt. Lett.* **13**, 47 (1988).
6. P. Yeh, "Coupled-mode theory of hologram sharing in mutually pumped phase conjugators," *Appl. Opt.* **28**, 1961 (1989).
7. M. Cronin-Golomb, B. Fischer, J. O. White, and A. Yariv, "Theory and applications of four-wave mixing in photorefractive media," *IEEE J. Quantum Electron.* **QE-20**, 12 (1984).
8. D. Wang, Z. Zhang, Y. Zhu, S. Zhang, and P. Ye, "Observations on the coupling channel of two mutually incoherent beams without internal reflections in BaTiO<sub>3</sub>," *Opt. Commun.* **73**, 495 (1989).
9. A. M. C. Smout and R. W. Eason, "Analysis of mutually incoherent beam coupling in BaTiO<sub>3</sub>," *Opt. Lett.* **12**, 498 (1987).
10. M. T. Gruneisen, E. D. Seeberger, J. F. Mileski, and K. Koch, "Effects of laser coherence on coupling efficiency for the double phase-conjugate mirror," *Opt. Lett.* **16**, 596 (1991).
11. Q. B. He and P. Yeh, "Photorefractive mutually-pumped phase conjugation with partially coherent beams," *Appl. Phys. B* **60**, 47 (1994).
12. R. S. Cudney, R. M. Pierce, G. D. Bacher, and J. Feinberg, "Absorption gratings in photorefractive crystals with multiple levels," *J. Opt. Am. B* **8**, 1326 (1991).
13. These mounts were provided by New Focus, Inc., 1275 Reamwood Avenue, Sunnyvale, Calif. 94089-2256.
14. D. Statman and B. Liby, "Two-beam cross coupling from mutually incoherent lasers," *J. Opt. Soc. Am. B* **6**, 1884 (1989).
15. K. R. MacDonald, J. Feinberg, M. Z. Zha, and P. Günter, "Asymmetric transmission through a photorefractive crystal of barium titanate," *Opt. Commun.* **50**, 146 (1984).
16. M. Zgonik, P. Bernasconi, M. Duelli, P. Schlessler, P. Günter, M. H. Garrett, D. Rytz, Y. Zhu, and X. Wu, "Dielectric, elastic, piezoelectric, electro-optic and elasto-optic, tensors of BaTiO<sub>3</sub> crystals," *Phys. Rev. B* **50**, 5941 (1994).
17. See, e.g., M. Born and E. Wolf, *Principles of Optics*, 6th ed. (Pergamon, New York, 1980), Chap. 10. Note that the symbol for mutual coherence is often  $\gamma$ .
18. Q. C. He, "Theory of photorefractive phase conjugators with mutually incoherent beams," *IEEE J. Quantum Electron.* **24**, 2507 (1988).

# Eminent Domains<sup>16</sup>

Ferroelectric crystals interact strongly with light and are used for optical memories, modulators, and switches. In such crystals, the unit cell has a front that differs from the back, and the lowest energy state is attained when all of the unit cells are aligned in the same direction, the  $c$  axis. In real materials, small groups of renegade cells cluster into domains where they align with each other but not with the rest of the crystal. If oriented  $180^\circ$  relative to the  $c$  axis, they cannot be detected except through elaborate or destructive procedures. S. MacCormack and J. Feinberg of the University of Southern California have devised a simple optical technique to image these domains. A probe laser beam sent through the crystal



shows a uniform image (A). If a second laser beam is simultaneously sent through the crystal, wherever the probe passes through an inverted domain, it loses energy to the second beam by the photorefractive effect (B). The researchers found that crystal samples believed to consist of only a single domain actually contained a large number of misoriented domains, a finding that may require the revision of existing values for the electrooptic coefficient of these materials. [Image

courtesy of S. MacCormack and J. Feinberg, Department of Physics, University of Southern California, Los Angeles, CA 90089-0484, USA. E-mail: feinberg@physics1.usc.edu]

# All-optical three-dimensional mapping of 180° domains hidden in a BaTiO<sub>3</sub> crystal

Victor Grubsky, Stuart MacCormack, and Jack Feinberg

Department of Physics, University of Southern California, Los Angeles, California 90089-0484

Received August 31, 1995

We present three-dimensional, high-contrast maps of 180° domains hidden inside photorefractive crystals of BaTiO<sub>3</sub>. Some domains are columns that run the entire length of the crystal, whereas others are short needles that begin predominantly on the  $-c$  surface but disappear inside the crystal bulk. © 1996 Optical Society of America

Photorefractive crystals of BaTiO<sub>3</sub> are widely used for optical storage, signal processing, and beam amplification. These applications all require high-optical-quality crystals that are free of domains (as described below). We present here an all-optical method to detect and map any domains hidden inside such crystals. We present three-dimensional maps showing these domains in glorious detail.

In the temperature range  $T = 9\text{--}125^\circ\text{C}$  BaTiO<sub>3</sub> is tetragonal, with each unit cell having a nonzero dipole moment,  $\mathbf{P}$ .<sup>1</sup> In as-grown crystals, neighboring cells form regions or domains with their polarizations  $\mathbf{P}$  all aligned in the same direction, but different domains may be aligned in any of three orthogonal directions. In a multidomain crystal the total spontaneous polarization averaged over the entire volume is approximately zero, making such a crystal useless for electro-optical and photorefractive applications. To produce a useful crystal, one must align all the domains so that their spontaneous polarizations  $\mathbf{P}$  all point in a common direction. Applying a dc electric field along one of the crystal axes causes the many domains to merge into a single domain that fills the entire crystal volume, and the direction of  $\mathbf{P}$  is called the crystal's  $c$  axis.

However, single-domain crystals of BaTiO<sub>3</sub> are a rarity. Surface cracks or defects in the crystal can pin a domain and prevent its unit cells from aligning with the applied electric field. Even after electrical poling, thermal or mechanical shock can cause domains to reappear in a previously perfect crystal.

In BaTiO<sub>3</sub> domains form with their  $\mathbf{P}$  aligned at either 90° or 180° to the crystal  $c$  axis, as shown in Fig. 1. The 90° domains are easily observed with the naked eye because of the  $\Delta n \sim 0.05$  refractive-index step at their domain boundary. One can also see 90° domains by viewing the crystal through crossed polarizers. In contrast, the 180° domains are invisible both to the naked eye and by viewing through crossed polarizers. 180° domains at the crystal's surface can be revealed by etching the crystal  $c$  faces with acids (such as HF and HCl),<sup>2</sup> and domains in the crystal's bulk can be seen by x-ray diffraction<sup>3</sup> or second-harmonic generation at the domain boundaries.<sup>4</sup> However none of these techniques is ideal, because they damage the crystal, require elaborate instruments, or have limited resolution.

In contrast to the above techniques, optical beam coupling<sup>5</sup> uses the difference in the sign of two-beam coupling to locate 180° domains embedded in a photorefractive crystal. Kahmann *et al.* used a beam-coupling geometry to detect large 180° domains present in a  $\text{Sr}_{1-x}\text{Ba}_x\text{Nb}_2\text{O}_6$  crystal.<sup>6</sup> Using a different geometry, MacCormack and Feinberg<sup>7</sup> and MacCormack *et al.*<sup>8</sup> revealed 180° domains averaged over the length of a BaTiO<sub>3</sub> crystal. Here we extend their imaging technique to produce a complete three-dimensional map of the 180° domains hidden in the bulk of a BaTiO<sub>3</sub> crystal.

Two light beams, a pump beam and a signal beam, couple inside the photorefractive crystal. The signal beam propagates precisely down the crystal's  $c$  axis. The crystal is oriented so that the signal beam loses energy to the pump beam. (This orientation minimizes the amount of pump light that is fanned in the direction of the transmitted signal beam.) Where the signal beam encounters a 180° domain the direction of its energy coupling is locally reversed, so that it gains energy from the pump beam. If the BaTiO<sub>3</sub> crystal were free of domains the signal beam would be uniformly depleted as the pump beam stole its energy. However, any 180° domains hidden in the crystal reveal themselves by producing bright spots on the otherwise depleted signal beam.

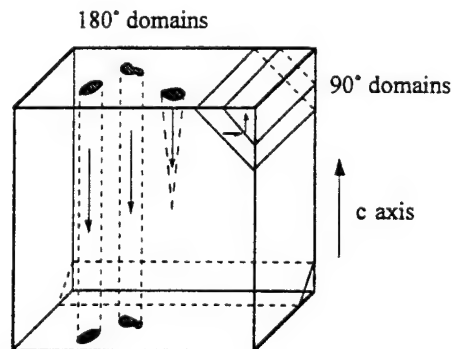


Fig. 1. Domains in BaTiO<sub>3</sub> crystals have their polarizations aligned either 90° or 180° to the crystal's  $c$  axis. The 90° domains tend to form at the corners and along the edges of the crystal, whereas the 180° domains prefer the bulk of the crystal.



We use here a narrow-width pump beam effectively to select only a narrow slice of the crystal, as beam coupling occurs only in regions where both the pump and the signal beams are present. Starting with the pump beam close to one  $c$  face of the  $\text{BaTiO}_3$  crystal, we translated the crystal, step by step, parallel to its own  $c$  axis to scan the pump beam along the length of the crystal. After each step an optical frame grabber stored the image of the transmitted signal beam.

In a previous experiment our pump beam filled the entire volume of the crystal, so the signal beam coupled with all the  $180^\circ$  domains in the entire crystal at the same time.<sup>7,8</sup> However, here we use the trick of focusing the pump beam to a thin vertical slice. Even though the probe beam traverses the entire crystal, it reveals only the domains in a thin slice of the crystal traversed by the pump beam. By changing the intersection point of the two light beams we generate a fresh crystal slice. If we think of the crystal as a chunk of Swiss cheese, our narrow pump beam effectively cuts the cheese into thin slices. Later we use image-processing software<sup>9</sup> to reassemble all the slices and construct a complete, three-dimensional map of the crystal's  $180^\circ$  domains, much as a computer-aided tomography scan reassembles a three-dimensional image of the body from two-dimensional slices.

Figure 2 shows the optical setup. A single-frequency  $\text{Ar}^+$  laser produced 150 mW of vertically polarized light at 514 nm. A half-wave plate rotated the light polarization to horizontal before a beam splitter divided the light into two beams: the pump and the signal beams. A variable-density filter in the path of the signal beam decreased its power to  $\sim 0.1\%$  of the pump beam's power. An  $f = -100$  mm lens expanded the signal beam to fill most of the crystal's volume. The signal beam entered the  $\text{BaTiO}_3$  crystal approximately normal to one of the crystal  $c$  faces, and the crystal was then adjusted so that the signal beam propagated along the  $c$  axis. The transmitted signal beam exited the crystal and was collected by an  $f = 50$  mm camera lens and imaged onto a CCD camera. An  $f = 50$  mm cylindrical lens focused the pump beam to a vertical line and into an  $a$  face of the crystal at an external incident angle of approximately  $45^\circ$ . The pump beam had a horizontal FWHM of  $320 \mu\text{m}$  at the entrance to the crystal.

We chose the width of the pump beam as a compromise between signal-to-noise ratio in the image and spatial resolution along the crystal  $c$  axis. A narrower pump beam would have cut thinner slices and so increased the spatial resolution along the  $c$  axis, but its decreased width would have reduced the power transferred into the signal beam and so reduced the signal-to-noise ratio of the image.

Figure 3 shows a signal beam transmitted through a nominally undoped  $\text{BaTiO}_3$  crystal with and without the tightly focused pump beam present. With the pump beam present the signal beam is depleted everywhere except in the  $180^\circ$  domains, where the signal beam is amplified. The domains stand out as bright spots on a dark background, with a contrast

ratio of  $\sim 25$  dB. The resulting intensity pattern is a two-dimensional slice showing the location of  $180^\circ$  domains inside the thin slice of crystal traversed by the pump beam.

Figure 3(a) also reveals a number of faint, small, square features in the transmitted signal beam, even with the pump beam absent. Inspecting this  $\text{BaTiO}_3$

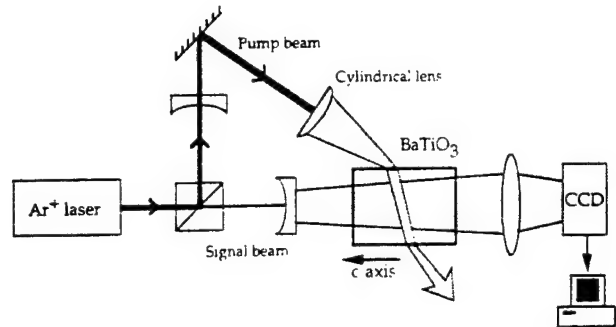


Fig. 2. Optical setup used to observe  $180^\circ$  domains hidden inside a  $\text{BaTiO}_3$  crystal. The crystal was translated in steps by a precision translation stage to select a different intersection plane of the pump and the signal beams. The transmitted signal beam revealed  $180^\circ$  domains present in each optical slice through the crystal; the camera (CCD) and the computer recorded each slice.

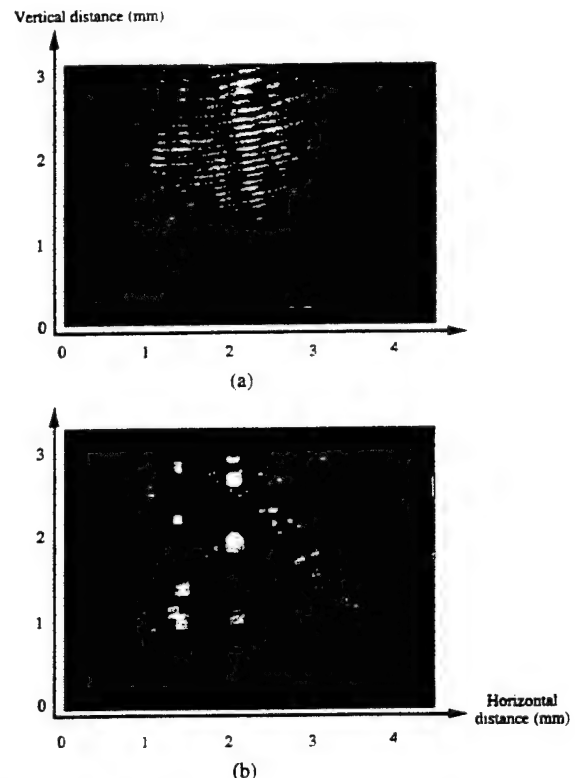


Fig. 3. Profile of the transmitted signal beam (a) with the pump beam absent and (b) with the pump beam switched on. Each bright square corresponds to a  $180^\circ$  domain. The fringes in (a) are due to the interference of multiple reflections from the crystal surface. (b) is one of 20 data slices, all orthogonal to the  $c$  axis, used to construct the three-dimensional map of the  $180^\circ$  domains inside the crystal seen in Fig. 5 below. The very small squares barely visible on the transmitted beam shown in (a) arise from phase steps etched by acids during crystal polishing.

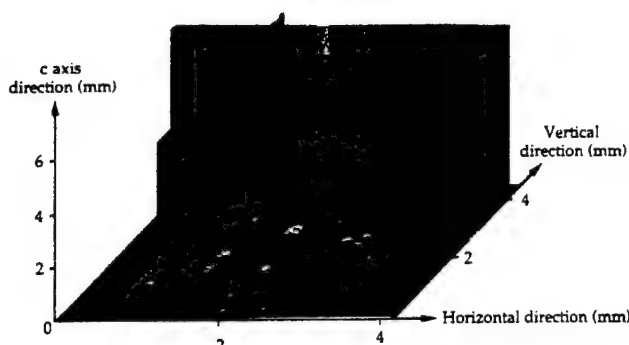


Fig. 4. Two reconstructed slices of the  $\text{BaTiO}_3$  crystal cut parallel to the crystal  $c$  axis. (These slices were reconstructed from 20 data slices as in Fig. 3.) One can see dagger domains starting at the  $c$  faces and tapering into the crystal. Also visible are pillar domains that run the entire length of the crystal's  $c$  axis.

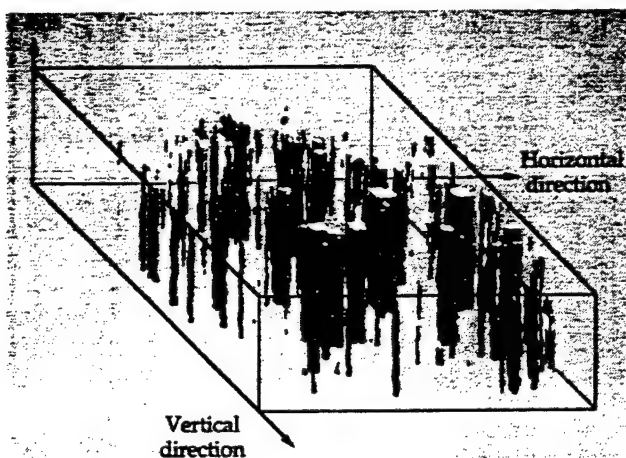


Fig. 5. Three-dimensional reconstruction of the domain structure inside a nominally undoped  $\text{BaTiO}_3$  crystal (FRANK). The  $c$ -axis length has been artificially compressed in this picture to make the distant domains more visible.

crystal under a light microscope, we saw a multitude of square steps on the  $(-c)$  face of the crystal. In our experiment these surface steps impart phase steps to the probe beam, which, after propagation, become the small, square intensity features seen in Fig. 3(a). Interestingly, we find that the locations of these surface steps exactly correlate with the positions of the  $180^\circ$  domains near that surface of the crystal. This suggests that domains were present in this particular crystal before its final polishing, so that during polishing the acidic polishing solution etched steps on the  $-c$  face precisely at the locations of the  $180^\circ$  domains.

Our  $\text{BaTiO}_3$  crystal, a nominally undoped crystal (named FRANK) purchased from Virgo Optics, was 6.6 mm long. We took 20 adjacent optical slices spaced  $250\ \mu\text{m}$  apart, and Fig. 4 shows the reassembled,

three-dimensional domain structure sliced in a perpendicular direction, that is, along the  $c$  axis of the crystal. The pattern of domains is in good agreement with the domain structures generally observed by other techniques.<sup>3</sup> We see two types of  $180^\circ$  domain: small needle domains that originate at a crystal surface and taper a short distance into the bulk of the crystal and pillar domains that run the entire length of the crystal with a fixed cross section. In this particular crystal the majority of its pillar domains appear to have rectangular cross sections, but such regular domain profiles are absent in other  $\text{BaTiO}_3$  crystals that we mapped. The finite pixel size of our CCD camera limited the spatial resolution perpendicular to the  $c$  axis to  $\sim 7\ \mu\text{m}$ .

Figure 5 shows a map of the three-dimensional domain structure reconstructed from our 20 two-dimensional slices. This domain map resembles that obtained by x-ray diffraction, but it does not require a synchrotron.<sup>3</sup>

In summary, we have presented an all-optical technique for seeing the three-dimensional structure of  $180^\circ$  domains hidden in the bulk of  $\text{BaTiO}_3$  crystal. This domain-mapping technique can be used with any photorefractive crystal that exhibits two-beam coupling. The technique is simple and nondestructive to crystals or budgets; with a laser and simple optics one can now map the domain structure of such crystals.

This research was supported in part by the U.S. Air Force Office of Scientific Research and the Joint Services Electronics Program.

## References

1. M. B. Klein, in *Photorefractive Materials and Their Applications I*, P. Günter and J.-P. Huignard, eds., Vol. 61 of Topics in Applied Physics (Springer-Verlag, Berlin, 1988).
2. F. Jona and G. Shirane, *Ferroelectric Crystals* (Pergamon, Oxford, 1962).
3. G. Fogarty, B. Steiner, M. Cronin-Golomb, U. Laor, R. Uhrin, and J. Martin, in *Digest of Topical Meeting on Photorefractive Materials, Effects and Devices* (Optical Society of America, Washington, D.C., 1995), paper MB1.
4. R. W. Hellwarth and P. Christensen, *Opt. Commun.* **12**, 318 (1974).
5. F. Kahmann, R. Matull, R. A. Rupp, and J. Seglins, *Europhys. Lett.* **13**, 405 (1990).
6. F. Kahmann, R. Matull, R. A. Rupp, and J. Seglins, *Phase Trans.* **40**, 171 (1992).
7. S. MacCormack and J. Feinberg, "Revealing  $180^\circ$  domains in ferroelectric crystals by photorefractive beam coupling," submitted to *Appl. Opt.*
8. S. MacCormack, J. Feinberg, and B. A. Wechsler, in *Digest of Topical Meeting on Photorefractive Materials, Effects and Devices* (Optical Society of America, Washington, D.C., 1995), paper MPB13.
9. Spyglass Dicer, Spyglass Inc., 1800 Woodfield Drive, Savoy, Illinois 61874.

# Revealing 180° domains in ferroelectric crystals by photorefractive beam coupling

Stuart MacCormack and Jack Feinberg

We describe a simple, optical technique for mapping 180° domains hidden inside photorefractive crystals. We intersect two coherent light beams in the crystal. Photorefractive coupling between the two beams causes one beam to emerge with a map of all the crystal's 180° domains imprinted upon it. We tested many BaTiO<sub>3</sub> crystals and found that they all contained 180° domains, with the relative volume of these domains varying from 25% to 0.1%. © 1996 Optical Society of America

When viewed from an airplane, an automobile parking lot appears to contain simple rectangles. However, closer inspection reveals that each rectangle has a front (with headlights) and a back (with brake lights). Similarly, in ferroelectric crystals each unit cell has a front and a back. Thermodynamically the lowest energy state of these crystals, such as BaTiO<sub>3</sub> and LiNbO<sub>3</sub>, has all the unit cells pointed in the same direction, creating a single domain throughout the crystal volume. However, in practice the unit cells cluster into domains. In each domain the unit cells have aligned with each other, but in different regions of the crystal the domains point in different directions. Here we present a powerful yet simple method for revealing such ferroelectric domains in photorefractive crystals.

Domains can be useful. Magnetic domains are manipulated in ferromagnetic tape to record music and video information. Electric domains are manipulated in ferroelectric crystals to store information for computer memories.<sup>1</sup> In photorefractive crystals ferroelectric domains can be created by light and will persist long after the light is removed, and so may prove useful for all-optical memories.<sup>2,3</sup> Before writing data into such a crystal one would like to begin with a blank page, i.e., with a single-domain crystal, where every unit cell points in the same direction. In most photorefractive applications one also wants a crystal free of all 180° domains. In optical signal processing and holographic data storage, the pres-

ence of 180° domains can lead to increased cross talk and reduced signal-to-noise ratio.

However, in practice we find that there are usually domains insidiously embedded throughout the volume of these crystals. In BaTiO<sub>3</sub> these domains always orient at 90° or 180° to the crystal's principal polar direction, called the +*c*-axis direction. Any 90° domains can be seen easily by eye, because at the domain boundary the crystal's refractive index undergoes a step of  $\Delta n = 0.04$ , and this is sufficiently large to scatter light into the viewer's eye. However any 180° domains are invisible.

One can reveal 180° domains in crystals by etching a *c* face of the crystal with acids (HF or HCl) that preferentially etch one unit cell orientation quicker than its 180° flipped orientation. Unfortunately, acid etching mottles the crystal's surface and so ruins the optical polish of the crystal's face. Repolishing the crystal often introduces new domains, which must then be revealed by acid etching, etc. [Acid etching of crystals is comparable to finding the front of an automobile by smashing its end with a hammer, listening for the tinkle of broken glass, and then seeing if the glass was clear (must have been the front) or red (must have been the back).] Additionally, acid etching reveals domains only at the surface of crystals and so cannot see domains hidden inside the crystal's bulk. It is possible for one to see into a crystal to a depth of 1–2 mm using x rays, but a synchrotron is required.<sup>4</sup>

Kahmann *et al.* used laser beams to map 180° domains in a (BaSr)Nb<sub>2</sub>O<sub>6</sub> crystal.<sup>5</sup> In their technique the pump and a probe beams both entered an *a* face of the crystal, but this smeared out the location of the 180° domains in one transverse direction. In contrast, we propagate our probe beam precisely along the *c* axis so that 180° domains are displayed without

The authors are with the Department of Physics, University of Southern California, Los Angeles, California 90089-0484.

Received 12 December 1995; revised manuscript received 4 March 1996.

0003-6935/96/305961-03\$10.00/0

© 1996 Optical Society of America



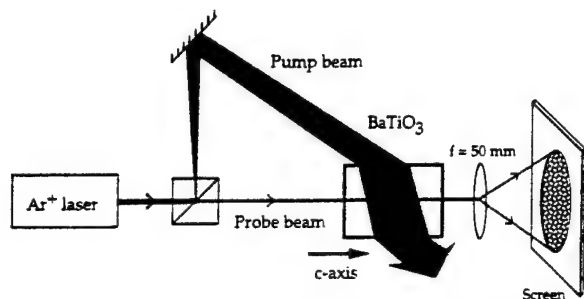


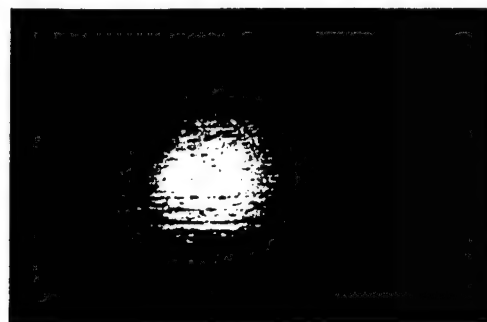
Fig. 1. Optical setup to observe  $180^\circ$  domains hidden inside a  $\text{BaTiO}_3$  crystal. A probe beam travels exactly along the crystal's  $c$  axis and steals energy from a pump beam by photorefractive two-beam coupling, except in crystal regions containing  $180^\circ$  domains. Any  $180^\circ$  domains hidden in the crystal appear as dark spots on the screen.

any transverse smearing. Although in the research presented here we cannot resolve domain structure along the crystal  $c$  axis, in Ref. 6 we presented a fully three-dimensional technique for mapping domains hidden in photorefractive crystals.

Our simple, all-optical method reveals  $180^\circ$  domains anywhere inside a photorefractive crystal and without harming the crystal. Figure 1 shows a probe laser beam that propagates along the crystal's  $c$  axis. We also direct a pumping laser beam into the crystal so that it intersects with the probe beam throughout most of the crystal volume. The external beam crossing angle is  $\sim 45^\circ$ , but the resulting image is relatively insensitive to the exact beam coupling geometry. A lens collects the transmitted probe beam and produces an image of the crystal on a suitably positioned screen. Both the pump and probe beams are extraordinarily polarized and coherent with each other in the crystal to maximize their two-beam coupling gain. In this experiment our light source is an  $\sim 100\text{-mW}$   $\text{Ar}^+$  laser operated at a wavelength of  $514\text{ nm}$ .

Figure 2(a) shows the transmitted probe beam with no pump beam present; the Gaussian intensity profile of the probe beam is evident. In Fig. 2(b) the pump beam has been turned on, and dark holes now appear to have been eaten into the probe beam. The image resembles a slice of Swiss cheese. These holes are caused by columns of  $180^\circ$  domains hidden in the volume of the crystal, with the axis of the column aligned parallel to the  $+c$  axis of the crystal. If the entire crystal is rotated so that the crystal's  $+c$  axis now points against the probe beam, the holes turn into bright spots, each spot again revealing the head of a  $180^\circ$  domain, as shown in Fig. 2(c).

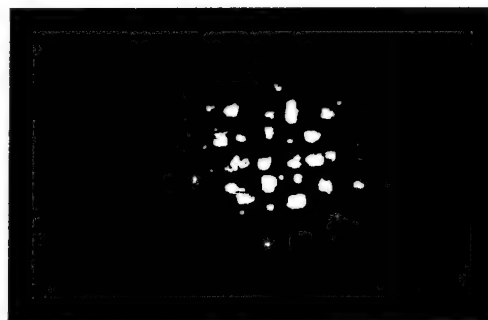
The explanation for this Swiss-cheese pattern is as follows. If the  $\text{BaTiO}_3$  crystal has no domains (and positive charges as its majority carrier), then as the probe beam travels along the  $c$  axis it gains energy from the pump beam by the photorefractive effect.<sup>7</sup> However, if the probe beam propagates through a  $180^\circ$  domain, then in that reversed region it loses energy to the pump beam. The probe beam then exits the crystal with dark holes eaten in it, and the



(a)



(b)



(c)

Fig. 2. Profile of the transmitted probe beam after it travels along the crystal's  $+c$ -axis direction: (a) with no pump beam present, (b) with the pump beam present, and (c) with the probe beam traveling against the  $c$ -axis direction. In (b) the domains appear as dark holes. In (c) the crystal has been rotated by  $180^\circ$  so the same domains now appear as bright spots. [Note: image (c) has been flipped left/right for ease of comparison with image (b).]

positions of the holes correspond to the locations of the  $180^\circ$  domains in the crystal, as in Fig. 2(b). If we rotate the crystal to flip the direction of the  $+c$  axis as in Fig. 2(c), then the probe beam loses energy in the bulk of the crystal except when it travels through a  $180^\circ$  domain, where it now gains energy. The probe beam is depleted by the pump beam everywhere except in the  $180^\circ$  domains, which makes the domains now appear as bright spots in an otherwise dark background.

To achieve good contrast in these domain maps, it is important that the probe beam propagate exactly along the axis of the  $180^\circ$  domains, i.e., along the  $c$  axis. If the crystal is slightly tilted, so that the probe beam no longer travels precisely along the  $c$  axis,

then the gain seen by different parts of the probe beam becomes averaged over regions of amplification and depletion, and this ruins the contrast between the domains and background. With the crystal properly aligned the minimum feature size that we observe is  $\sim 25 \mu\text{m}$ . These small features are the first to blur when the crystal is rotated, typically disappearing for crystal misalignment  $\theta > 1^\circ$ . (Note that this alignment technique can be used to locate accurately a crystal's  $c$  axis.) The larger features, which are as large as  $500 \mu\text{m}$  in diameter, persist at misalignments to  $\theta \sim 12^\circ$ , but their finer detail is lost.

We used this technique to image the  $180^\circ$  domains in eight supposedly single-domain  $\text{BaTiO}_3$  crystals. These crystals were grown in a number of different laboratories in the United States and China, and they contained a wide range of dopants. Surprisingly, we saw  $180^\circ$  domains in every crystal. The fraction of the crystal's volume occupied by these domains varied from  $\sim 25\%$  (for the crystal shown in Fig. 2) to  $< 0.1\%$  for our cleanest crystal. Using such crystals for optical storage would have produced excessive cross talk. The use of such crystals in photorefractive beam coupling experiments would have yielded incorrect values for any of the crystal's electro-optic coefficients. The ubiquitous presence of domains in all our crystals certainly casts doubt on the accuracy of experimentally measured values of the electro-optic coefficients in  $\text{BaTiO}_3$  and may explain the widely disparate values obtained by different experimenters. Researchers should first check their crystals for  $180^\circ$  domains using our simple technique before using that crystal in a quantitative experiment.

We have presented a simple but powerful technique for revealing the precise spatial location and shape of a crystal's  $180^\circ$  domains, both those intentionally created for the storage of data and those

inadvertently created by thermodynamics. Photorefractive beam coupling produces a map of the domain structure in two dimensions and can reveal domains with widths as small as  $\sim 20 \mu\text{m}$ . All the supposedly single-domain samples of  $\text{BaTiO}_3$  that we tested contained  $180^\circ$  domains. By applying a voltage across the crystal, we can also observe the complicated dynamics of domain formation and motion in real time.

This research was funded by the U.S. Air Force Office of Scientific Research.

## References

1. F. Micheron and G. Bismuth, "Electrical control of fixation and erasure of holographic patterns in ferroelectric materials," *Appl. Phys. Lett.* **20**, 79–81 (1972); "Field and time thresholds for the electrical fixation of holograms recorded in  $(\text{Sr}_{0.75}\text{Ba}_{0.25})\text{Nb}_2\text{O}_6$  crystals," *Appl. Phys. Lett.* **23**, 71–72 (1973).
2. M. Horowitz, A. Bekker, and B. Fischer, "Image and hologram fixing method with  $\text{Sr}_x\text{Ba}_{1-x}\text{Nb}_2\text{O}_6$  crystals," *Opt. Lett.* **18**, 1964–1966 (1993).
3. J. F. Heanue, M. C. Bashaw, and L. Hesselink, "Volume holographic storage and retrieval of digital data," *Science* **265**, 749–752 (1994).
4. G. Fogarty, B. Steiner, M. Cronin-Golomb, U. Laor, R. Uhrin, and J. Martin, in *Digest of Topical Meeting on Photorefractive Materials, Effects, and Devices* (Optical Society of America, Washington, D.C., 1995), pp. 9–12.
5. F. Kahmann, R. Matull, R. A. Rupp, and J. Seglins, "Polarization topography in photorefractive ferroelectrics," *Europhys. Lett.* **13**, 405–410 (1990); "A new method for the study of antiparallel ferroelectric domains," *Phase Transitions* **40**, 171–185 (1992).
6. V. Grubsky, S. MacCormack, and J. Feinberg, "All-optical three-dimensional mapping of  $180^\circ$  domains hidden in a  $\text{BaTiO}_3$  crystal," *Opt. Lett.* **21**, 6–8 (1996).
7. J. Feinberg, D. Heiman, A. R. Tanguay, Jr., and R. W. Hellwarth, "Photorefractive effects and light-induced charge migration in barium titanate," *J. Appl. Phys.* **51**, 1297–1305 (1980); erratum **52**, 537 (1981).

# Measurement of the phase of second-harmonic generation in SK5 glass

Vince Dominic,\* Patrick Lambelet, and Jack Feinberg

Departments of Physics and Electrical Engineering, University of Southern California,  
University Park, Los Angeles, California 90089-0484

Received September 16, 1994

Focusing an intense laser beam and its second harmonic into a SK5 glass slab transforms the glass into a frequency doubler. We present a new method to measure the optical phase between the second-harmonic beam that transformed the glass and the second-harmonic beam subsequently generated by the glass. We find this phase shift to be  $\Delta\theta = -90^\circ \pm 7^\circ$ . A spatial map of this phase confirms that the internal dc electric field locked inside the glass resembles a dipole electric field.

Frequency doubling in glass should be forbidden, because glass has macroscopic inversion symmetry. However, in 1986 Österberg and Margulis<sup>1</sup> observed frequency doubling in a glass optical fiber after illuminating the fiber with intense infrared light for several hours. A year later Stolen and Tom<sup>2</sup> showed that launching some frequency-doubled green light into a fiber along with the infrared light dramatically increased the speed of the process, from 10 h to 5 min. It is now understood that the incident fundamental and frequency-doubled light beams cause a dc electric field to build up in the glass and that this semipermanent dc electric field not only breaks the inversion symmetry of the glass but also permits periodic phase matching of the frequency-doubling process.<sup>3-5</sup>

Here we measure the relative phase shift  $\Delta\theta$  between the frequency-doubled green beam used to seed the glass and the frequency-doubled green beam generated inside the glass. Why is this phase shift worth measuring? Because it provides a check on the validity of current theories of second-harmonic generation in glass. Recent experiments<sup>6-8</sup> have measured these two green beams to be out of phase by  $90^\circ$ , which, at first glance, is precisely the wrong value for this process to be able to bootstrap up and grow in strength. (Adding a small vector at  $90^\circ$  to an existing vector only rotates the vector's direction but does not increase its magnitude.) We find that, in fact, the phase  $\Delta\theta$  is near  $-90^\circ$  in our Schott SK5 glass sample. However, even with  $\Delta\theta = -90^\circ$ , the seeding process's finite time response can permit exponential growth of the dc electric field with time.<sup>9-11</sup>

We present a new technique to measure the phase shift between the seeding and the glass-generated green light beams. Our technique is similar to the methods discussed in Refs. 6-8, except that, as shown in Fig. 1, we use *three* frequency-doubling elements to avoid perturbing the original seeding beam, namely: (i) a doubling crystal [lithium triborate (LBO)] located before the glass sample, which makes the original green seeding beam, (ii) the glass sample, which creates the green signal beam, and (iii) another doubling crystal [potassium titanyl phosphate (KTP)] located after the glass sample, which provides a green reference beam. In order to determine the relative phase of beams (i) and (ii), we

measure two separate interference patterns, namely, (a) that between beams (i) and (iii) and (b) that between beams (ii) and (iii). The phase shift  $\Delta\theta$  between the green seed (i) and the green signal (ii) is then obtained from the relative displacement of the two interference patterns (a) and (b).

Notice that, instead of attenuating the seeding green beam, we simply block it and replace it with the infrared seeding beam, which we then double in a KTP crystal after the infrared light has passed through the glass sample. Any phase shift imparted by the green-blocking filter to the infrared beam then appears on both the SK5-generated and the KTP-generated second-harmonic beams and so is automatically canceled.

We use a mode-locked (76-MHz repetition rate) and Q-switched (1-kHz pulse rate) Nd:YAG laser (Coherent Antares). Some of the infrared ( $\lambda = 1.064 \mu\text{m}$ ) light from the laser is frequency doubled in a LBO crystal that is noncritically phase matched, so that the green and the infrared beams follow the same optical path, as shown in Fig. 1. The polarization of the infrared and the green seeding beams is vertical, and we adjust their powers to 3 W and 2 mW, respectively. At the focus these powers correspond to  $4 \times 10^{11}$  and  $4 \times 10^8 \text{ W/cm}^2$  of peak power for the infrared and the green beams, respectively. We seed a virgin location in our Schott SK5 sample for 10 min. We then acquire interference pattern (a) be-

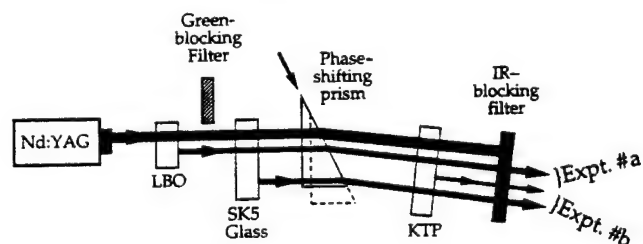


Fig. 1. Second-harmonic light generated in the KTP crystal interferes with that generated in either (a) the LBO crystal (green-block filter removed) or (b) the seeded SK5 glass sample (green-block filter present). Translating the glass prism shifts the phase of the green beam (from either LBO or SK5) compared to that of the green beam from the KTP crystal. The direction of the prism's arrow corresponds to the positive axis of Fig. 2.

tween the green beams generated in the LBO and KTP crystals by translating a prism and sampling the intensity pattern as it sweeps past our apertured detector. (For the beam power and exposure time used, the green generated by the SK5 sample is too weak to affect this interference pattern; the ratio of the glass-produced green and the LBO-produced green is less than  $10^{-3}$ ). We then block the green seeding beam from the LBO crystal with a green-blocking-infrared-passing filter. We measure interference pattern (b) of the green beams generated by the glass sample and by the KTP crystal, as shown in Fig. 2. (We are careful always to return the prism to its original position and eliminate backlash.) Because the green beam generated in the KTP crystal is common to both interference patterns (a) and (b), comparing these two interference patterns reveals the phase shift between the LBO-generated green (the seeding beam) and the SK5-generated green (the glass signal beam). We measured this phase shift twelve times and found an average phase shift  $\Delta\theta = -90^\circ \pm 7^\circ$ , where the minus means that the glass-produced green beam is in advance of the seeding green beam (as previously observed by Koch and Moore<sup>7</sup>).

Our technique is insensitive to nonlinear-optical phase shifts caused by self-phase modulation and cross-phase modulation so long as the infrared power is the same for both fringe-shift measurements. This is because any self-phase modulation of the infrared beam or cross-phase modulation of the infrared on the green beam will be common to both interference patterns (a) and (b) and so will cancel. Unfortunately, when we insert our green-blocking filter to eliminate the LBO-generated green and acquire interference pattern (b) we unavoidably decrease the infrared power by 10%. To check the importance of this effect, we seeded the glass sample and then measured the phase shift with different powers for the infrared reading beam. We observed a slight phase-shift dependence of  $2^\circ/\text{W}$ , which imparted a negligible error ( $<1^\circ$  of phase shift) to our experiments.

Recent theories of second-harmonic generation in glass make different predictions for how the phase shift  $\Delta\theta$  measured here will vary with the transverse position of the probing beam.<sup>12,13</sup> Therefore we varied the position of the probing beam to construct a spatial map of the phase shift  $\Delta\theta$ , as follows. First we seeded one spot in the glass sample, using  $\hat{y}$ -polarized green and infrared beams. We then probed at different locations, using a single  $\hat{y}$ -polarized infrared probing beam and translating the sample perpendicular to the direction of the probing beam. Figure 3 shows that the measured phase shift remained  $\Delta\theta = -90^\circ$  in the center of the seeded spot and along a horizontal scan through the center but underwent an abrupt step of  $180^\circ$  as we scanned in the vertical direction. This dependence of  $\Delta\theta$  on the position of the probing beam is precisely that expected if the electric field locked in the crystal (and causing the glass's frequency doubling) comes from the dipole field shown in Fig. 4.<sup>12</sup> Imagine probing this transverse dc field pattern near its center, where the dc electric field is directed up (+y direction). In

this central region the y component of this dipole dc electric field points up everywhere; however, if the probing beam is moved sufficiently above or below the edges of the dipole, the y component abruptly switches sign and points down. Switching the sign of the dc electric field imparts an extra  $180^\circ$  phase shift to the green beam generated in the glass sample [as we show in Eq. (2) below] and so causes the abrupt phase jumps seen in the data of Fig. 3. In contrast, translating the probe beam horizontally along the center-line scans a y component of the dc field that

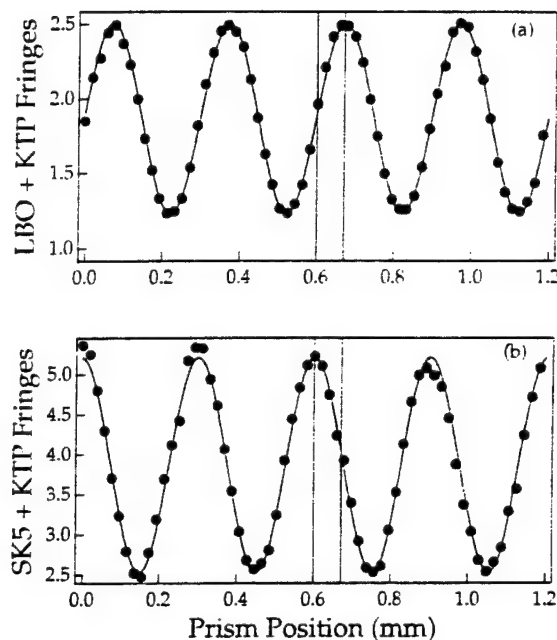


Fig. 2. (a) By translating a phase-shifting glass prism, we map out the interference pattern between the green beams from the LBO and KTP crystals. (b) We then block the green seeding beam (from the LBO crystal) and measure the interference pattern between the green beams from the SK5 glass sample and the KTP crystal. The phase shift between these two patterns gives the desired phase shift  $\Delta\theta$  between the seeding and the generated green beams in the SK5 glass sample.

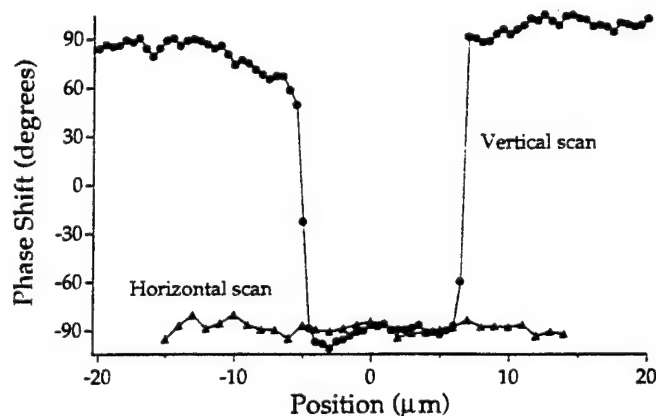


Fig. 3. Measured phase shift  $\Delta\theta$  versus the probing beam position near the center (position 0) of the seeded spot. For a horizontal scan (triangles) the phase shift is independent of the position. However, for a vertical scan (circles) the phase shift experiences  $180^\circ$  jumps on the outskirts of the seeding light beams, where the dc dipole electric field reverses sign (see Fig. 4).

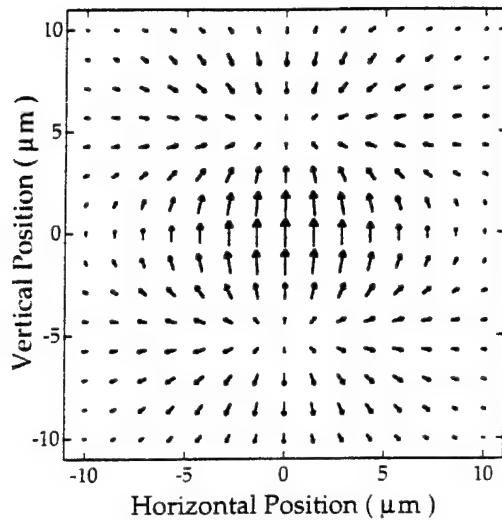


Fig. 4. Shape of the light-induced dc electric field transverse to the direction of the seeding beams when both of the seeding beams are vertically polarized (from Ref. 12). Note that along the vertical axis of symmetry ( $x = 0$ ) the dc field switches direction from up to down at the outskirts of the dipole pattern, near  $y = \pm 6 \mu\text{m}$ . In contrast, along the horizontal axis of symmetry ( $y = 0$ ) the dc field points up everywhere. This dipole electric field explains the phase-shift data seen in Fig. 3.

always points in the same direction ( $+y$ ). Therefore we expected and observed no jumps in the measured phase shift  $\Delta\theta$  as we scanned the horizontal position of the probing beam in the glass, as shown in Fig. 3. Notice that the  $x$  component of the dc electric field is negligible along centered horizontal and vertical scans, so it does not affect the measured phase. We measured the same phase map even when we reduced the green seeding intensity by a factor of 200, which was the lower limit for our detection system.

In these experiments the intensity of the glass-generated green is always much less than that of the LBO-generated green that seeded the glass. Therefore the LBO-generated green beam sets the phase of the dc field in the glass, and the weak, glass-generated green beam does not affect its own generation. In this case, the seeding fields at  $\omega$  and  $2\omega$  create a dc electric field in the glass given by<sup>2</sup>

$$E_{dc} = \Gamma E_{\omega}^* E_{2\omega}^* E_{2\omega}^{LBO} \exp[i(k_{2\omega} - 2k_{\omega})z] \\ = |\Gamma| E_{\omega}^* E_{\omega}^* E_{2\omega}^{LBO} \exp[i(k_{2\omega} - 2k_{\omega})z + i\phi_r], \quad (1)$$

where  $z$  is the direction of light propagation,  $\Gamma$  is the growth rate constant,  $\phi_r$  is the spatial phase shift between the three-field interference term and the dc electric field, and  $E_{2\omega}^{LBO}$  is the optical field of the green seeding beam. We wish to determine  $\phi_r$ . The coupled-wave equation for dc-field-induced second-harmonic generation is

$$\frac{dE_{2\omega}^{glass}}{dz} = i \frac{3\omega}{2n_{2\omega}c} \chi^{(3)} E_{dc} E_{\omega} E_{\omega} \exp[i(2k_{\omega} - k_{2\omega})z]. \quad (2)$$

Inserting Eq. (1) into Eq. (2) and keeping only the phase-matched terms in the interaction, we find that

$$\frac{dE_{2\omega}^{glass}}{dz} = i \frac{3\omega}{2n_{2\omega}c} \chi^{(3)} |\Gamma| |E_{\omega}|^2 E_{2\omega}^{LBO} \exp(i\phi_r). \quad (3)$$

The measured phase shift  $\Delta\theta$  between the glass-generated green and the LBO-generated seeding green will be  $\Delta\theta = \phi_r + 90^\circ$  because of that factor of  $i$  in Eqs. (2) and (3). Our measurements yield a value  $\Delta\theta = -90^\circ$ , which implies that  $\phi_r = -180^\circ$ , so that the dc field induced inside the SK5 glass is spatially in phase with the three-field interference term  $-E_{\omega}^{*2} E_{2\omega}$ . This result confirms the spatially local response seen in Ge-doped fused silica<sup>6,7</sup> and in the Soviet glass ZhS-4.<sup>8</sup>

Compared with previous techniques, our experimental technique offers several advantages for studying the phase of the frequency-doubled light generated by glass. Because we do not disturb the seeding beam, we can map out the phase at different locations in the sample. We observe a  $180^\circ$  discontinuity in the phase of the green light generated in the glass sample as we move the optical probe toward the edge of the seeded region in the vertical direction but not in the horizontal direction. These results confirm that the original green and infrared seeding beams create a dipole-like charge distribution in the glass.

This research was supported by grant F49620-92-J-0022 of the U.S. Air Force Office of Scientific Research (AFOSR) and by the Joint Services Electronics Program. Vince Dominic thanks the AFOSR Summer Faculty Research Program and the Materials Directorate at Wright-Patterson Air Force Base for their support.

\*Present address, Center for Electro-Optics, University of Dayton, Dayton, Ohio 45469-0245.

## References

1. U. Österberg and W. Margulis, *Opt. Lett.* **11**, 516 (1986); **12**, 57 (1987).
2. R. H. Stolen and H. W. K. Tom, *Opt. Lett.* **12**, 585 (1987).
3. V. Dominic and J. Feinberg, *Phys. Rev. Lett.* **71**, 3446 (1993).
4. V. Mizrahi, Y. Hibino, and G. Stegeman, *Opt. Commun.* **78**, 283 (1990).
5. E. M. Dianov, P. G. Kazansky, D. S. Starodubov, and D. Yu. Stepanov, *Sov. Lightwave Commun.* **2**, 83 (1992).
6. W. Margulis, I. C. S. Carvalho, and J. P. von der Weid, *Opt. Lett.* **14**, 1346 (1989).
7. K. Koch and G. T. Moore, *Opt. Lett.* **16**, 1436 (1991).
8. M. A. Bolshtyansky, V. M. Churikov, Yu. E. Kapitzky, A. Yu. Savchenko, and B. Ya. Zel'dovich, *Opt. Lett.* **18**, 1217 (1993).
9. V. L. Vinetskii, N. V. Kukhtarev, S. G. Odulov, and M. S. Soskin, *Sov. Phys. Usp.* **22**, 742 (1979).
10. E. M. Dianov, P. G. Kazanskii, and D. Yu. Stepanov, *Sov. J. Quantum Electron.* **20**, 849 (1990).
11. M. I. Dyakonov and A. S. Furman, *Electron. Lett.* **27**, 1429 (1991).
12. V. Dominic and J. Feinberg, *Opt. Lett.* **18**, 784 (1993).
13. T. J. Driscoll and N. M. Lawandy, *J. Opt. Soc. Am. B* **11**, 355 (1994).



# Phase of second-harmonic light self-generated in a glass fiber

Patrick Lambelet\* and Jack Feinberg

Department of Physics, University of Southern California, Los Angeles, California 90089-0484

Received January 1, 1996

Focusing an intense laser beam and its second harmonic into a glass fiber transforms the fiber into a frequency doubler. We measure the temporal evolution of both the amplitude and the phase of the second-harmonic light produced by a germanium-doped fiber and so determine the initial phase of the second-harmonic light to be  $\Delta\theta = -71^\circ \pm 3^\circ$ . We demonstrate that the fiber-produced green light can exceed the seeding green light even if these two beams are  $90^\circ$  out of phase. We also show that cross-phase modulation in the fiber can limit the maximum useful interaction length and consequently the ultimate efficiency of second-harmonic generation in fibers. © 1996 Optical Society of America

Because glass has macroscopic inversion symmetry, frequency doubling in glass should be forbidden. However, Österberg and Margulis<sup>1</sup> observed frequency doubling in a glass optical fiber after illuminating the fiber with intense infrared light at  $\lambda = 1.06 \mu\text{m}$  for several hours. A year later Stolen and Tom<sup>2</sup> showed that launching some frequency-doubled green light into the fiber along with the infrared light decreased the required irradiation time from 10 h to 5 min. It is now understood that the incident fundamental and frequency-doubled light beams cause a dc electric field to spring up in the glass. This semipermanent dc electric field not only ruins the inversion symmetry of the glass and so permits the glass to be a frequency doubler but also causes periodic phase matching of the frequency-doubling process.<sup>3-5</sup>

Returning to the experiments of Refs. 1 and 2, how did their fibers grow to become efficient frequency doublers? The key factor is the phase  $\Delta\theta_0$  between the green light that seeds the nonlinearity and the green light produced by this nonlinearity.<sup>6-8</sup> Our previous measurement in SK-5 glass bulk samples<sup>9</sup> gave a phase difference  $\Delta\theta_0 = -90^\circ$ , where the minus means that the glass-produced green beam is in advance of the seeding green beam (as previously observed by Koch and Moore<sup>6</sup>). At first glance, a phase shift of  $\Delta\theta_0 = -90^\circ$  is precisely the wrong value to use to allow a weak green seeding beam to grow in strength, because adding a small vector at  $90^\circ$  to an existing vector only rotates the vector's direction but does not increase its magnitude. However, we show below that the finite response time of the fiber's transformation allows it to grow in strength even if the initial phase shift is  $\Delta\theta_0 = -90^\circ$ .<sup>10,11</sup>

We used a germanium-doped glass fiber with a step index  $\Delta n = 5 \times 10^{-3}$  that is single mode in both the green and the infrared. Our Nd:YAG laser was mode locked and Q switched (Coherent Antares, 76-MHz pulse rate, 1-kHz repetition rate,  $\lambda = 1.064 \mu\text{m}$ ). Some of the laser's infrared light was frequency doubled in a lithium triborate (LBO) crystal that was non-critically phase matched, so the green and the infrared beams followed exactly the same optical path, as shown in Fig. 1. Using an achromatic lens, we coupled the incident light beams into a 25-mm-long fiber. Both the

infrared and the green beams were vertically polarized, and their average incident powers were, respectively, 500 and 0.1 mW on our power monitor.

We first tried to measure the phase difference  $\Delta\theta_0$  between the seeding green and the fiber-generated green by extending to fibers the technique that proved successful with bulk glass samples.<sup>9</sup> Briefly, we interfere a green seeding beam generated in the LBO crystal with a green reference beam generated by frequency doubling the transmitted infrared light in a potassium titanyl phosphate (KTP) crystal placed after the fiber, as shown in Fig. 1. We translate a prism and record intensity interference pattern 1 as it sweeps past our apertured detector. We then block the green seeding beam from the LBO crystal with a green-blocking-infrared-passing filter and slightly boost the infrared power to compensate for the 10% loss induced by the filter for this wavelength. We now interfere the green beams generated in the fiber and the KTP crystal to record a different interference pattern, 2. Comparing the two interference patterns reveals any phase shift  $\Delta\theta_0$  between the seeding and the fiber-generated green beams. However, six measurements in our Ge-doped fiber (each time with a new fiber) gave a wide spread of values with a mean value  $\Delta\theta_0^{\text{Ge fiber}} = -75^\circ \pm 15^\circ$ .

The large spread in the measured value of  $\Delta\theta_0$  was caused by the high intensity of our infrared light beam, which induced both self-phase and cross-phase modulation in our 25-mm-long fibers.<sup>12</sup> To

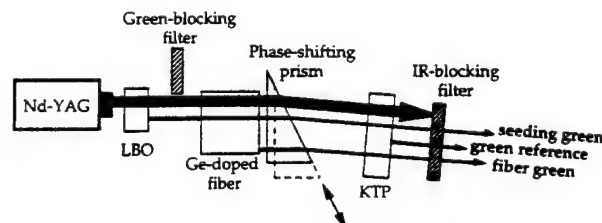


Fig. 1. Setup for determining the phase of the green light generated in the fiber with respect to the green seeding light from the LBO crystal. Translating the dispersive prism shifts the relative phase of the green beam (either LBO-generated or fiber-generated) compared with that of a common phase-reference green beam from the KTP crystal.<sup>9</sup>

demonstrate the importance of cross-phase modulation in our experiments we varied the power of the infrared reading beam and measured the phase of the fiber-produced green from a previously prepared fiber. Figure 2 shows our plot of the measured phase  $\theta$  of the fiber-produced green relative to the KTP-produced green versus the incident power of the reading beam,  $P_\omega$ . In this plot we arbitrarily set  $\theta = 0^\circ$  when the reading beam power meter read  $P_\omega = 0.5$  W, which was the power that the beam had when it wrote the grating. The measured phase clearly varied with power of the reading beam and with a measured slope of  $530^\circ/\text{W}$ .

We find the predicted variation of phase with the intensity  $I_\omega$  in the fiber by letting the infrared field with amplitude  $E_\omega$  at frequency  $\omega$  and the green field with amplitude  $E_{2\omega}$  at frequency  $2\omega$  propagate in the single-mode fiber with wave vectors  $k_\omega = (\omega/c)(n_\omega + n_2 I_\omega)$  and  $k_{2\omega} = (2\omega/c)(n_{2\omega} + 2n_2 I_\omega)$ , respectively. Here  $n_\omega$  and  $n_{2\omega}$  are the effective linear refractive indices for the infrared and the green beams in the fiber and  $c$  is the speed of light. The nonlinear index  $n_2$  causes self-phase modulation of the infrared beam on itself and cross-phase modulation of the infrared beam on the green beam. (We neglect nonlinearities induced by the weak beam.) Integrating Eq. (1b) below and using the appropriate wave vectors for the green and the infrared beams yields  $\Delta\theta^{\text{fiber}} = n_2 I_\omega \omega L/c$ , where  $n_2$  is the nonlinear index of the glass fiber and  $L$  is its length. To determine the peak intensity in the fiber we measured the  $1/e^2$  intensity radius of the mode in the fiber to be  $3.7 \mu\text{m}$  for the infrared (and  $1.4 \mu\text{m}$  for the green). The duration of each mode-locked pulse was 180 ps (FWHM), with  $\sim 22$  such pulses contained in the full width of the  $Q$ -switched envelope (280 ns FWHM). We measured a 30% coupling efficiency into the fiber for both wavelengths. Only 40% of the infrared power was in pulses; the rest was ineffective, prelude dribble from the  $Q$  switcher. From the above data we calculate that  $P_\omega = 1$  W on our infrared powermeter corresponds to a peak intensity of  $I_\omega = 1.3 \times 10^{11} \text{ W/cm}^2$  in the fiber. Substituting<sup>13</sup>  $n_2 = +3.2 \times 10^{-16} \text{ cm}^2/\text{W}$  predicts a slope in Fig. 2 of  $\sim 350^\circ/\text{W}$ , which is in reasonable agreement with our measured slope of  $530^\circ/\text{W}$ . This large slope means that in a fiber even a small change in the effective infrared light intensity can drastically alter the measured phase shift  $\Delta\theta_0$ . This problem was absent in our phase measurements in glass bulk samples because of the short interaction length ( $L \approx 0.1 \text{ mm}$ ) in those experiments.<sup>9</sup>

Therefore we devised a new method to measure the phase  $\Delta\theta_0$  in fibers that is relatively immune to the effects of cross- and self-phase modulation: We measure how the phase of the green light emanating from the fiber changes with time. As before, we used a 25-mm-long Ge-doped fiber that produced no detectable green light without seeding. We then measured the evolution of the phase [Fig. 3(a)] and the power [Fig. 3(b)] of the total green light coming out of the fiber. At time  $t = 0$ , only the seeding beam was present, and we arbitrarily set its phase to  $\theta = 0^\circ$ . Figure 3 shows that, as the fiber slowly transformed itself into a frequency doubler, the fiber-generated green light was added to the seeding green light to change the total phase of the

green light to  $\theta = -50^\circ$  and to increase the total power of the green light by a factor of 1.7.

To understand the data of Fig. 3 and to extract the initial phase  $\Delta\theta_0$  we use two nicely coupled differential equations.<sup>10,11</sup> By the interference of multiphoton excitations the two light fields generate a dc electric field  $E_{dc}$  inside the fiber.<sup>14,15</sup> The differential equations for (a) the evolution of this dc electric field  $E_{dc}$  with time and (b) the slowly varying amplitude  $E_{2\omega}$  of the green

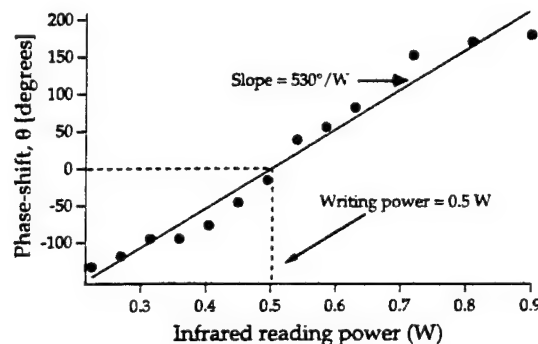


Fig. 2. Variation of the measured phase  $\theta$  of the fiber-produced green light for different reading infrared powers  $P_\omega$ . For  $P_\omega = 0.5$  W (which corresponds to powermeter setting during writing), we set  $\theta = 0^\circ$ . As we change the infrared reading power, the phase  $\theta$  varies as the result of nonlinear phase modulation in the fiber. This effect eventually limits the efficiency of frequency doubling in a long fiber.

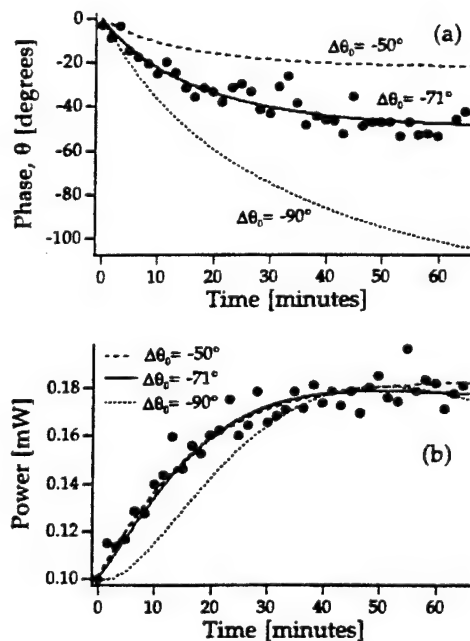


Fig. 3. Measurement of (a) the phase and (b) the power of the total green light (seed plus fiber-generated) from the fiber during seeding. The curves are theoretical fits from Eqs. (1). We tried  $\Delta\theta_0 = -50^\circ$  (dashed curves),  $\Delta\theta_0 = -71^\circ$  (solid curves), and  $\Delta\theta_0 = -90^\circ$  (dotted curves). We used the growth rate coefficient  $\beta$  and the photoconductivity  $\sigma$  of the glass as free parameters. At time  $t = 0$ , only the seeding light is present, and the green phase is  $\theta = 0^\circ$  by convention.

beam with distance are

$$\frac{\delta E_{dc}}{\delta t} + \frac{\sigma}{\epsilon \epsilon_0} E_{dc} = \beta E_{2\omega} (E_w^*)^2 \times \exp[i(k_{2\omega} - 2k_w)z + \phi_\beta] + \text{c.c.}, \quad (1a)$$

$$\frac{\delta E_{2\omega}}{\delta z} = i \frac{3\omega}{2cn_{2\omega}} \chi^{(3)} E_{dc} (E_w)^2 \exp[-i(k_{2\omega} - 2k_w)z]. \quad (1b)$$

Here  $\sigma$  is the photoconductivity of the material; it is essentially zero in the absence of light and is responsible for saturation of the process.  $\beta$  determines the growth rate of the dc electric field,  $n_{2\omega}$  is the index of refraction for the green light,  $c$  is the speed of light, and  $\chi^{(3)}$  is the third-order nonlinear coefficient of the material. In principle the phase  $\phi_\beta$  can arise from the difference in the phases of the bound and the free wave functions of the ejected electrons.<sup>14,15</sup> The initial phase shift  $\Delta\theta_0$  between the fiber-generated green and the seeding green is then  $\Delta\theta_0 = \phi_\beta + 90^\circ$  because of that factor of  $i$  just after the equal sign in Eq. (1b).

We numerically integrate Eqs. (1), using laser pulse amplitudes that vary in time like the pulses from our mode-locked, Q-switched laser. By fitting our data of Fig. 3 to the coupled differential equations (1) we could determine the initial phase shift  $\Delta\theta_0$  in the fiber. For each choice of  $\Delta\theta_0$  we varied the growth rate coefficient  $\beta$  and the photoconductivity  $\sigma$  to obtain the best fit. The three different curves in each graph correspond to different values of the initial phase difference between the seeding and the fiber-produced green:  $\Delta\theta_0 = -50^\circ$  (dashed curves),  $\Delta\theta_0 = -71^\circ$  (solid curves), and  $\Delta\theta_0 = -90^\circ$  (dotted curves). Whereas in Fig. 3(b) the three curves are too similar to allow us to determine  $\Delta\theta_0$ , Fig. 3(a) clearly shows that  $\Delta\theta_0 = -71^\circ \pm 3^\circ$  gives the best fit, in good agreement and with a factor-of-5 less uncertainty than for our directly measured value  $\Delta\theta_0^{\text{Ge fiber}} = -75^\circ \pm 15^\circ$  measured above. For this graph the growth rate  $\beta = 4.7 \times 10^{-17} [\text{V}^{-2} \text{m}^{-2} \text{s}^{-1}]$  and the photoconductivity  $\sigma = 4.2 \times 10^{-14} [\text{AV}^{-1} \text{m}^{-1}]$  were the optimum values for these fitting parameters. The nonlinear effects that plagued our direct measurements of  $\Delta\theta_0$  are largely eliminated here because  $I_w$  is writing and reading at the same time and so has the same value during both processes. This causes the  $n_2$  nonlinearities largely to cancel, as one can see by comparing Eqs. (1a) and (1b). Indeed, we found that setting  $n_2 = 0$  in Eqs. (1) changed our best-curve-fit value of  $\Delta\theta_0$  by only  $1^\circ$ .

Equations (1) and Fig. 3(b) demonstrate that, even if the initial phase shift between the seeding and the fiber-produced green beams had been  $-90^\circ$ , the power of the fiber's green light could nevertheless have grown in time. As this is being written, the dc-field-induced grating changes the phase of the green light linearly with distance along the fiber, and, because it takes the grating a finite time to respond to changes in the light beams, the two green beams are no longer in quadrature, allowing the total green power to grow. If the initial phase shift differs from  $\Delta\theta_0 = -90^\circ$ , then the green light can grow more rapidly.

When we tried experiments in a fiber ten times longer ( $L = 250 \text{ mm}$ ), we found that the green and the infrared beams were relatively incoherent after traversing the fiber; that is, we could not observe any stable interference fringes between the KTP-produced and the fiber-produced green beams. The coherence length of our green-light pulses measured by a Michelson interferometer was  $L_{\text{coh}} = 8.4 \text{ mm}$  (HWHM); the measured coherence length of our infrared light pulses was even longer at  $19.5 \text{ mm}$  (HWHM). After a 250-mm fiber is traversed, group-velocity dispersion predicts a walk-off of only  $\Delta L = 5.7 \text{ mm}$ , so our infrared and green beams had not walked off here. The culprit was the factor-of-2 difference between cross- and self-phase modulation; it makes the relative phase of the infrared and the green beams rapidly shift during each infrared laser pulse. Toward the far end of the fiber this rapid phase shift smeared the multiphoton interference grating into oblivion. In agreement with Kapitzy and Zel'dovich,<sup>12</sup> we find that the nonlinear refractive index of glass prevents nonsquare pulsed light beams from converting a long length of glass fiber into a high-efficiency frequency doubler.

This research was supported in part by grant F49620-94-0022 of the Joint Services Electronics Program and F49620-95-1-0082 of the U.S. Air Force Office of Scientific Research.

\*Present address, Laboratoire d'Optique Appliquée, Département de Microtechnique, Ecole Polytechnique Fédérale, CH-1015 Lausanne, Switzerland.

## References

1. U. Österberg and W. Margulis, *Opt. Lett.* **11**, 516 (1986); **12**, 57 (1987).
2. R. H. Stolen and H. W. K. Tom, *Opt. Lett.* **12**, 585 (1987).
3. V. Mizrahi, Y. Hibino, and G. Stegeman, *Opt. Commun.* **78**, 283 (1990).
4. E. M. Dianov, P. G. Kazansky, D. S. Starodubov, and D. Yu. Stepanov, *Sov. Lightwave Commun.* **2**, 83 (1992).
5. V. Dominic and J. Feinberg, *Phys. Rev. Lett.* **71**, 3446 (1993).
6. K. Koch and G. T. Moore, *Opt. Lett.* **16**, 1436 (1991).
7. W. Margulis, I. C. S. Carvalho, and J. P. von der Weid, *Opt. Lett.* **14**, 700 (1989).
8. M. A. Bolshtyansky, V. M. Churikov, Yu. E. Kapitzy, A. Yu. Savchenko, and B. Ya. Zel'dovich, *Opt. Lett.* **18**, 1217 (1993).
9. V. Dominic, P. Lambelet, and J. Feinberg, *Opt. Lett.* **20**, 444 (1995).
10. E. M. Dianov, P. G. Kazanskii, and D. Yu. Stepanov, *Sov. J. Quantum Electron.* **20**, 849 (1990).
11. M. I. Dyakonov and A. S. Furman, *Electron. Lett.* **27**, 1429 (1991).
12. Yu. E. Kapitzy and B. Ya. Zel'dovich, *Opt. Commun.* **78**, 227 (1990).
13. R. H. Stolen and C. Lin, *Phys. Rev. A* **17**, 1448 (1978).
14. N. B. Baranova, A. N. Chudinov, A. A. Shulginov, and B. Ya. Zel'dovich, *Opt. Lett.* **16**, 1346 (1989).
15. D. Z. Anderson, V. Mizrahi, and J. E. Sipe, *Opt. Lett.* **16**, 796 (1991).



# Anisotropy of the hole drift mobility in barium titanate

Daniel Mahgerefteh,\* Dimitri Kirillov,<sup>†</sup> Roger S. Cudney,<sup>‡</sup> G. David Bacher, Robert M. Pierce,<sup>§</sup> and Jack Feinberg  
*Departments of Physics and Electrical Engineering, University of Southern California, Los Angeles, California 90089-0484*  
 (Received 5 July 1995)

The static dielectric tensor is highly anisotropic in the tetragonal phase of barium titanate: the static dielectric constant perpendicular to the  $c$  axis,  $\epsilon_{\perp}$ , is 40 times that parallel to the  $c$  axis,  $\epsilon_{\parallel}$ , at  $T=20^{\circ}\text{C}$ , with this ratio decreasing to  $\sim 20$  times at  $T=90^{\circ}\text{C}$ . Using both holographic and bulk measurements we show that the hole drift mobility has comparable anisotropy: the hole mobility perpendicular to the  $c$  axis,  $\mu_{\perp}$ , is 20 times larger than that parallel to the  $c$  axis,  $\mu_{\parallel}$ , at  $T=20^{\circ}\text{C}$ , with this ratio decreasing to 8 times at  $T=90^{\circ}\text{C}$ . We also show that  $\mu_{\parallel}/\mu_{\perp} \sim 2\epsilon_{\parallel}/\epsilon_{\perp}$  independent of temperature between  $T=20^{\circ}\text{C}$  and  $T=90^{\circ}\text{C}$ , suggesting that the hole drift mobility in barium titanate crystals scales with the static dielectric constant in this temperature range.

Between  $\sim 10$  and  $\sim 125^{\circ}\text{C}$  barium titanate is a tetragonal, ferroelectric insulator, with highly anisotropic dielectric and electro-optical properties. In 1986, Tzou, Chang, and Hellwarth found that the mobility of holes in  $\text{BaTiO}_3$  crystals was also highly anisotropic at room temperature: the mobility perpendicular to the  $c$  axis,  $\mu_{\perp}$ , was 20 times larger than the mobility parallel to the  $c$  axis,  $\mu_{\parallel}$ .<sup>1</sup> Curiously, the static dielectric tensor has the same slant; the dielectric constant perpendicular to the  $c$  axis,  $\epsilon_{\perp}$ , is larger than the dielectric constant parallel to the  $c$  axis,  $\epsilon_{\parallel}$ , by a factor of 40. Although the anisotropy of the crystal properties is not unexpected, it is surprising that the hole drift mobility is higher in the direction with the higher dielectric constant and by nearly the same factor. Is this a coincidence, or is the mobility proportional to the dielectric constant in barium titanate?

One way to investigate a possible correlation between the mobility and the dc dielectric constant in barium titanate is to see how these quantities vary with temperature. Barium titanate has phase transitions at  $125$  and  $10^{\circ}\text{C}$  that are associated with soft phonon modes polarized parallel or perpendicular to the  $c$  axis, so the dielectric constants show a large variation over this temperature range. We therefore extended Tzou, Chang, and Hellwarth's measurements to the temperature range  $T=20$ – $90^{\circ}\text{C}$ , over which the ratio of the dielectric constants varies by a factor of 4;  $\epsilon_{\perp}$  decreases by a factor of 2, while  $\epsilon_{\parallel}$  increases by a factor of 2. We found that the ratio of mobilities parallel and perpendicular to the  $c$  axis indeed follows the ratio of dielectric constants in the two directions;  $\mu_{\parallel}/\mu_{\perp} \sim 2 \times \epsilon_{\parallel}/\epsilon_{\perp}$  over the measured temperature range. To ensure that the measured variations are not an impurity-dependent effect, we repeated these experiments in three barium titanate samples with widely different photoconductive properties. The same relation held in all three. Our results suggest that there is some fundamental connection between the static dielectric constant and drift mobility in barium titanate. To the best of our knowledge, no theory predicts this.

Drift mobility values derived from a measurement of photoconductivity are suspect because they depend on a precise knowledge of the density of carriers. Here we remove this ambiguity by measuring the ratio of mobilities, which is independent of the carrier density. We measured the hole mo-

bility ratio  $\mu_{\perp}/\mu_{\parallel}$  in barium titanate crystals using two methods: a straightforward measurement of the crystal's photoconductivity using electrodes placed on the crystal, and a holographic measurement that required no electrodes and instead used the photorefractive effect.

In our holographic experiments we interfere two light beams inside the crystal to create a spatially periodic intensity pattern. The light rearranges charges between deep trapping sites in a crystal. Impurities, vacancies, or defects in the crystal act as charge donors and acceptors. In nominally undoped barium titanate crystals, holes are the dominant charge carriers.<sup>2</sup> Once excited by light, the holes drift and diffuse through the crystal until they are retrapped. The holes are excited out of the bright regions and collect in the darker regions. The dc electric field of the resulting periodic charge pattern distorts the crystal lattice, and so creates a spatially periodic change in the crystal's index of refraction by the Pockels effect. We monitor the strength of this refractive-index grating by its diffraction of a separate light beam incident at the Bragg angle. We then make this grating decay by exposing it to an intense, uniform beam of light while recording its decay with time.

According to the single-trap-level theory of the photorefractive effect, at a temperature  $T$  the erasure rate of a photorefractive grating illuminated by a uniform beam of intensity  $I$  is given by<sup>3</sup>

$$\Gamma = \frac{e\mu n_0}{\epsilon} (1 + k_g^2/k_0^2), \quad (1)$$

where  $\mu(T)$  is the microscopic mobility,  $\epsilon(T)$  is the dielectric constant,  $k_0(T)$  is the Debye screening wave vector along the direction of charge migration,  $k_g$  is the magnitude of the grating wave vector, and  $e$  is the electric charge. The intensity dependence of Eq. (1) is hidden in the factor  $n_0(I, T)$ , the density of photocarriers. Equation (1) is approximately valid even if more than one trap level contributes to the crystal's photoconductivity, as long as  $n_0$  and  $k_0$  are calculated using a multiple-trap model.<sup>4</sup>

We measured the light-induced erasure rates  $\Gamma$  of photorefractive gratings oriented parallel or perpendicular to the  $c$  axis at a fixed light intensity and as a function of tempera-

ture, in three well-characterized BaTiO<sub>3</sub> samples. We previously measured values of the Debye screening wave vector  $k_0$  for both orientations of these three crystals at room temperature. In the present experiments we chose the grating wave vector  $k_g = 1.49 \mu\text{m}^{-1}$  to be small, so that the quantity in parentheses in Eq. (1) would be insensitive to variations in  $k_0$  with temperature. From our measurements of  $k_0$  and the grating erasure rates  $\Gamma$ , we determined the dielectric relaxation rates  $e\mu n_0/\epsilon$  parallel and perpendicular to the crystal's  $c$  axis. For both the  $k_g \parallel \hat{c}$  and  $k_g \perp \hat{c}$  experiments, the erasing light had the same intensity and was polarized to be perpendicular to the  $c$  axis, so that the density of free carriers  $n_0(I, T)$  was the same for both crystal orientations. Consequently,  $n_0(I, T)$  conveniently cancels out when we take the ratio  $R$  of the measured dielectric relaxation rates parallel and perpendicular to the  $c$  axis:

$$R = \frac{\mu_{\parallel}/\epsilon_{\parallel}}{\mu_{\perp}/\epsilon_{\perp}} = \frac{\Gamma_{\parallel}(1 + k_g^2/k_{0\perp}^2)}{\Gamma_{\perp}(1 + k_g^2/k_{0\parallel}^2)}. \quad (2)$$

We used four-wave mixing to measure the photorefractive grating decay rates  $\Gamma_{\parallel}$  and  $\Gamma_{\perp}$  in three well-characterized BaTiO<sub>3</sub> crystals named Swiss, Free, and Chip, chosen for their different photoconductive properties. The Swiss crystal has a small dark conductivity (dark-storage time  $> 8$  h), and a photoconductivity  $\sigma_{\text{photo}} \sim I^{0.9}$  that scales nearly linearly with intensity at room temperature.<sup>5</sup> In contrast, the Free crystal has a relatively large dark conductivity (dark-storage time  $\sim 3$  s), and a photoconductivity that scales as  $\sigma_{\text{photo}} \sim I^{0.68}$  at room temperature.<sup>5</sup> The Chip crystal has a long dark-storage time and a photoconductivity that scales as  $\sigma_{\text{photo}} \sim I^{0.9}$ ; however, unlike the other two crystals, it shows hologram fixing.<sup>6</sup> The distinct photoconductive properties of these samples are determined by the densities and types of deep and shallow traps in each crystal.

The erasure rates were measured as follows. Two coherent writing beams intersected in the crystal at an angle  $2\theta = 7^\circ$  in air. This crossing angle is large enough so that effects of photogalvanic currents are negligible,<sup>7</sup> and small enough so that the grating wave vector is much smaller than the Debye screening wave vector. At room temperature in these crystals, we obtained  $(1 + k_g^2/k_{0\parallel}^2) = 1.0$  and  $(1 + k_g^2/k_{0\perp}^2) = 1.4$  for the Swiss crystal, and  $(1 + k_g^2/k_{0\parallel}^2) = 1.0$  and  $(1 + k_g^2/k_{0\perp}^2) = 1.2$  for the Free crystal.<sup>8</sup> For the Chip crystal  $(1 + k_g^2/k_{0\parallel}^2) \sim 1.0$ , and  $(1 + k_g^2/k_{0\perp}^2) = 1.2$ . An intense erasing beam, incoherent with the writing beams, flooded the crystal at all times. After a photorefractive grating was written to steady state, we caused the photorefractive grating to decay by rapidly vibrating one of the writing beam's mirrors, thereby ruining the interference pattern inside the crystal. This trick of keeping the erasing beam on continuously eliminated large transients in the photoconductivity of the crystal, although it decreased the peak strength of the photorefractive grating. The crystal was oriented so as to make the grating wave vector either parallel or perpendicular to the  $c$  axis. The intensities of the writing beams were  $I_1 = 0.2 \text{ W/cm}^2$  and  $I_2 = 0.049 \text{ W/cm}^2$ , and the intensity of the erasing beam was  $I = 4.0 \text{ W/cm}^2$ . All of these optical beams were at 514.5 nm and polarized perpendicular to the  $c$  axis of the crystal for both orientations of the crystal. The crystal

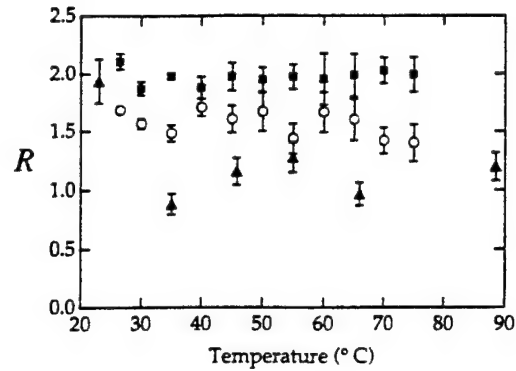


FIG. 1. Ratio  $R$  of the dielectric relaxation rates parallel and perpendicular to the  $c$  axis vs temperature in three barium titanate crystals: Swiss (full squares), Free (open circles), and Chip (full triangles).

temperature was stabilized to  $\pm 0.2^\circ \text{C}$ . The photorefractive grating was monitored by a weak, extraordinary-polarized beam from a He-Ne laser at  $\lambda = 632.8 \text{ nm}$  incident at the Bragg angle.

For the Swiss and Free crystals the decay of the diffracted signal fit well to a single exponential decay, and the erasure rate  $\Gamma$  was taken to be the inverse of the  $1/e$  decay time. For the Chip crystal the grating decay was best fit to a double exponential decay, with the two time constants differing by a factor of 100 or more. (The slower decay is thought to be caused by ionic motion.<sup>6</sup>) Here we take the erasure rate as the inverse of the  $1/e$  time constant of the faster decay.

Figure 1 shows the ratio  $R$  of the measured decay rates for gratings oriented parallel and perpendicular to the  $c$  axis in our three barium titanate crystals as a function of temperature. Note that  $R$  is approximately independent of temperature in this temperature range. For the Swiss crystal  $R_{\text{Swiss}} = 2.0 \pm 0.1$ , and for the Free crystal  $R_{\text{Free}} = 1.6 \pm 0.1$ . In the Chip crystal  $R_{\text{Chip}} = 1.1 \pm 0.1$  between 35 and 90  $^\circ \text{C}$ , but deviates to  $R \sim 2$  for  $T = 23^\circ \text{C}$ .

It surprised us that  $R$  was relatively constant with temperature even though, according to the literature<sup>9</sup> and to our experiments, both of the dielectric constants in Eq. (2) change markedly with temperature. Consequently, we performed an independent measurement of  $R$  by separately measuring the dielectric constant and the photoconductivity parallel and perpendicular to the  $c$  axis in one of the barium titanate crystals. We attached silver paste electrodes to opposite faces of the Chip crystal and applied  $\sim 5$ –50 V while illuminating it from the side by an  $I = 0.29 \text{ W/cm}^2$ , ordinary-polarized optical beam at 514.5 nm. The crystal temperature was controlled to better than  $\pm 0.1^\circ \text{C}$ . At each temperature and before each measurement the crystal was allowed to come to equilibrium to ensure that any transient pyroelectric currents had thoroughly decayed. The photocurrent through the crystal was measured by a Keithley Model 617 programmable electrometer. To avoid complications from photogalvanic currents when measuring the photoconductivity along the  $c$  axis, we measured the differential conductivity as follows. The applied voltage was slowly stepped at 5-V intervals from  $-50$  to  $+50$  V and back to  $-50$  V, and the current was measured. The conductivity of the crystal was deter-

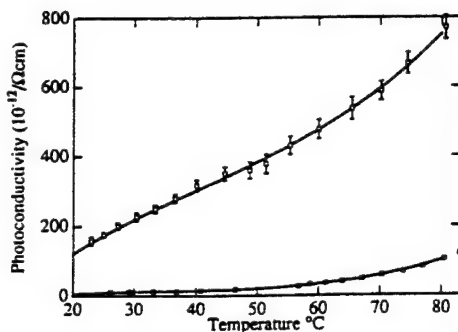


FIG. 2. Measured photoconductivity  $\sigma = e\mu n_0$  in the Chip crystal of barium titanate: parallel to the  $c$  axis (full squares), perpendicular to the  $c$  axis (empty squares). The lines are curve fits, which we use to generate Fig. 4.

mined from the slope of the current versus voltage ( $I$ - $V$ ) curve. We used the same method to measure the conductivity perpendicular to the  $c$  axis. The  $I$ - $V$  curve for the crystal was linear for applied voltages less than 100 V. The static dielectric constant was measured by applying a voltage to the crystal in the dark, assuming that it formed a parallel plate capacitor, and measuring the accumulated charge with the electrometer.

Figure 2 shows the measured values for the photoconductivity  $\sigma = e\mu n_0$ , and Fig. 3 the dielectric constant  $\epsilon$  both parallel and perpendicular to the  $c$  axis in the Chip crystal. Note that the photoconductivity perpendicular to the  $c$  axis is larger than the photoconductivity parallel to the  $c$  axis; the photoconductivity is larger in the direction having the larger dielectric constant. This agrees with our observation that the photorefractive erasure rate is nearly the same for gratings aligned parallel and perpendicular to the  $c$  axis. The increase in the photoconductivities along both directions with increasing temperature is caused in part by the increase in the photocarrier density with temperature.<sup>5</sup> Hence the temperature dependence of mobilities cannot be determined from these data.

Figure 4 compares the ratio  $R$  of the dielectric relaxation rates  $e\mu n_0/\epsilon$  parallel and perpendicular to the Chip crystal's  $c$  axis computed by two different methods. We obtain the triangular data points from our grating decay measurements (Fig. 1). We obtain the shaded region from our bulk measure-

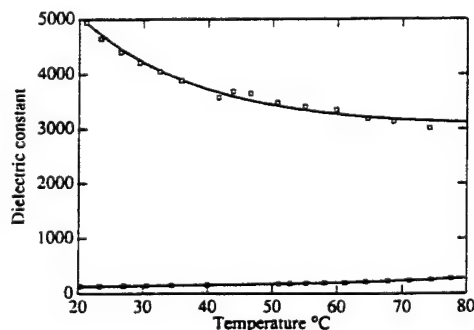


FIG. 3. Measured dc dielectric constant  $\epsilon$  in the Chip crystal of barium titanate parallel to the  $c$  axis (full squares), perpendicular to the  $c$  axis (empty squares). The lines are curve fits, which we use to generate Fig. 4.

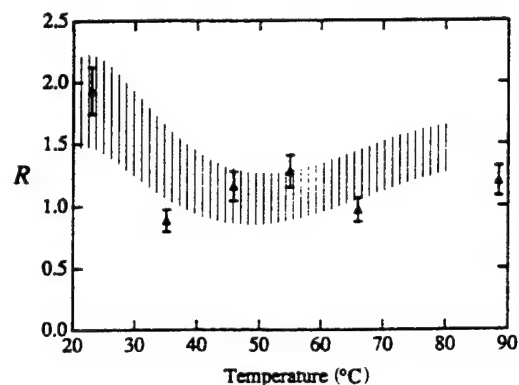


FIG. 4. The ratio  $R$  of dielectric relaxation rates  $e\mu n_0/\epsilon$  parallel and perpendicular to the  $c$  axis of the Chip crystal: holographic measurement (full triangles); bulk measurement (shaded region).

ments of the photoconductivities and dielectric constants; we empirically fit smooth curves through the data in Figs. 2 and 3, and then formed the ratio of these four curves to obtain  $R_{\text{bulk}} = \sigma_{\parallel} \epsilon_{\perp} / \sigma_{\perp} \epsilon_{\parallel}$ . The vertical extent of the shaded region in Fig. 4 reflects the uncertainties in our measurements of the photoconductivities and the dielectric constants. The holographic and electrical measurements are in good agreement.<sup>10</sup>

We did not repeat the electrical measurements of  $R$  in the other two crystals because this method is more difficult and, since it involves the surface of the crystal, less reliable than the holographic technique. Also, electrical measurements require good crystal surface quality, which was lacking on one crystal.

Our data in three different samples of barium titanate give a ratio  $R$  of dielectric relaxation rates that is relatively independent of temperature over the range  $T = 20$ – $90$  °C, even though in this temperature range  $\epsilon_{\parallel}$  doubles while  $\epsilon_{\perp}$  decreases by a factor of 2. To keep the ratio  $R$  independent of temperature, the mobilities must behave according to

$$\frac{\mu_{\parallel}(T)}{\mu_{\perp}(T)} = R \times \frac{\epsilon_{\parallel}(T)}{\epsilon_{\perp}(T)}. \quad (3)$$

From these data we conclude that the hole mobility is proportional to the dielectric constant, thereby keeping the ratio  $R$  relatively independent of temperature. It is interesting to note that Wemple, Di Domenico, and Jayaraman have found the seemingly opposite trend,  $\sigma = 1/\epsilon + \text{const}$ , in cubic  $n$ -type semiconducting barium titanate at 140 °C.<sup>11</sup> They arrived at this conclusion indirectly by showing that conductivity increased while dielectric constant decreased with increasing hydrostatic pressure. They explained their results based on a band picture with electron-TO-phonon interaction as the dominant scattering mechanism that determines the mobility. They did not carry out measurements or make predictions for the tetragonal phase of barium titanate.

Figure 5 shows a separate measure of the ratio of mobilities  $\mu$  in the Chip crystal; here we measure the photoconductivities directly in the two directions and plot their ratio  $\sigma_{\perp}/\sigma_{\parallel} = (e\mu_{\perp}n_0/e\mu_{\parallel}n_0) = \mu_{\perp}/\mu_{\parallel}$ . This ratio decreases from a value of 20 at  $T = 20$  °C to a value of 8 at  $T = 90$  °C, so the mobilities appear to approach the same value as the temperature is increased toward the tetragonal-

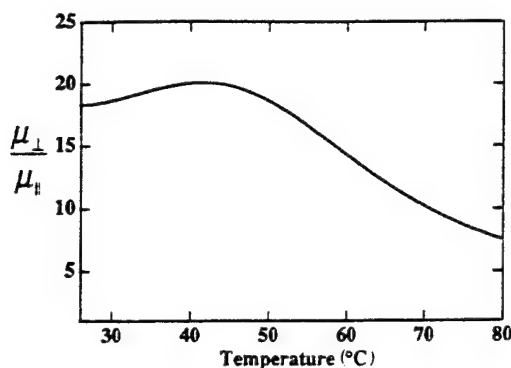


FIG. 5. The ratio  $\mu_{\perp}/\mu_{\parallel}$  of hole mobilities perpendicular and parallel to the  $c$  axis computed from the ratio  $\sigma_{\perp}/\sigma_{\parallel}$  of the measured photoconductivities in the Chip crystal of barium titanate.

to-cubic phase transition at  $T \sim 125^{\circ}\text{C}$ . Previous conductivity and Hall measurements by Berglund and Baer<sup>12</sup> in  $n$ -type conducting barium titanate showed a temperature-dependent anisotropy for electron drift mobility that is similar to our results for photogenerated holes.

The anisotropy in the hole drift mobility in barium titanate and its apparent connection with the dielectric constant is not satisfactorily explained by any theory. All of the previous work on mobilities in barium titanate is on electron transport in semiconducting crystals,<sup>11-14</sup> and, even then, there is no consensus on a theory. Berglund and Baer explain the electron mobility anisotropy based on a many-valley band conduction model,<sup>12</sup> while Girshberg, Bursian, and Grushevsky explain the same results based on a small-polaron hopping model.<sup>13</sup> As we explain below, neither model seems satisfactory for hole transport.

Band transport is not an appropriate description for hole conduction in barium titanate. According to band-transport models, a charge is assumed to move as a free particle of effective mass,  $m^*$ , in the crystal between collisions with phonons. However, this picture breaks down for crystals with low carrier mobility where the "scattering" length calculated from the Drude model,  $l_s \sim m^*v/\mu e$  becomes comparable to the de Broglie wavelength of the electron,  $\lambda_D \sim h/m^*v$ . Assuming the carrier is moving at the thermal velocity,  $v \sim \sqrt{3k_B T/m^*}$ , and taking its effective mass to be the free-electron mass, we find that at room temperature  $\lambda_D/l_s \geq 1$ , and band transport breaks down for  $\mu \leq 90 \text{ cm}^2/\text{V s}$ . The measured values of the hole mobility in barium titanate range from  $10^{-4}$  to  $0.5 \text{ cm}^2/\text{V s}$  (Ref. 3), so a band-transport model is clearly not valid.

A more appropriate model considers the carriers to be localized "small" polarons. A polaron is formed when a free electron or hole is injected into a polarizable lattice. The lattice distorts around the free carrier and traps it, forming a polaron. The steady-state mobility of the small polaron is given for a one-dimensional case by<sup>15</sup>

$$\mu = (ea^2\omega/2\pi k_B T)P \exp(-E_A/k_B T), \quad (4)$$

where  $\omega$  is the vibration frequency of the lattice,  $e$  is electric charge, and  $a$  is the lattice constant. The activation energy  $E_A$  is the minimum energy required to strain the neighboring

lattice sites and dig a potential well of appropriate depth for the hole. The jump probability (given the coincidence of energy levels) is given by<sup>15</sup>

$$P = 2\pi J^2/\hbar\omega(4E_A k_B T/\pi)^{1/2}, \quad (5)$$

where  $J$  is the overlap integral of the electronic wave functions of the adjacent sites. Girshberg, Bursian, and Grushevsky<sup>13</sup> explained the anisotropy of electron mobility based on the anisotropy of the overlap integral in Eq. (5). They reasoned that for highly localized wave functions the overlap integral can be assumed to vary exponentially with the lattice constant:

$$J \propto e^{-a/r_0}, \quad (6)$$

where  $r_0$  is the localization length. Using this form in Eqs. (4) and (5) for the steady-state mobility of the small polaron, the ratio of mobilities is given by

$$\frac{\mu_{\parallel}}{\mu_{\perp}} \propto \frac{J_{\parallel}^2}{J_{\perp}^2} \propto \exp\{2[a_{\perp}(T) - a_{\parallel}(T)]/r_0\}. \quad (7)$$

At room temperature the lattice constant of tetragonal barium titanate parallel to the  $c$  axis is larger than that perpendicular to the  $c$  axis, so by this argument one expects the mobility parallel to the  $c$  axis to be smaller than the mobility perpendicular to the  $c$  axis, in agreement with measurements by Berglund and Baer<sup>12</sup> and Girshberg, Bursian, and Grushevsky<sup>13</sup> as well as our direct measurements of photoconductivity. As the temperature increases toward the tetragonal-to-cubic phase transition, the barium titanate lattice shrinks parallel to the  $c$  axis and stretches perpendicular to the  $c$  axis (and approaches a cube at the transition temperature  $T \sim 125^{\circ}\text{C}$ ). According to Eq. (6) the wave-function overlap and the resulting mobility should increase parallel to the  $c$  axis and decrease perpendicular to the  $c$  axis. This is also in agreement with our data. Despite its appeal and apparent agreement with experimental results, this argument leads to an unphysical localization length. The lattice constants of barium titanate parallel and perpendicular to the  $c$  axis differ by  $\sim 0.04 \text{ \AA}$  at room temperature. For this difference to produce the measured hole mobility anisotropy of 20, we calculate from Eq. (7) that the polaron would have to be localized to  $r_0 \sim 0.03 \text{ \AA}$ .<sup>12</sup> This seems unphysical, considering that the ionic radii are at least an order of magnitude larger in barium titanate. In addition this reasoning does not relate mobility to the dielectric constant. It is curious, however, that the dependence in Eq. (7) closely matches our measurements of mobility anisotropy as a function of temperature.

Another plausible, yet unsatisfactory, explanation uses the dependence of the overlap integral in Eq. (5) on the nuclear motion of adjacent sites.<sup>16,17</sup> At any finite temperature the lattice is in motion about its equilibrium position, making excursions of order

$$\Delta x \sim \sqrt{2k_B T/M\omega_0^2}, \quad (8)$$

where  $M$  is the reduced mass of the vibrating ions. The larger the excursions, the closer adjacent lattice sites are on the average, and the larger become the overlap integral and the mobility. The connection to the dc dielectric constant



# Powerful, diffraction-limited semiconductor laser using photorefractive beam coupling

Stuart MacCormack, G. D. Bacher, and Jack Feinberg

*Department of Physics, University of Southern California, Los Angeles, California 90089-0484*

Steve O'Brien and Robert J. Lang

*SDL, 80 Rose Orchard Way, San Jose, California 95134*

Marvin B. Klein and Barry A. Wechsler

*Hughes Research Laboratories, 3011 Malibu Canyon Road, Malibu, California 90265*

Received August 20, 1996

We use semiconductor laser amplifiers and a photorefractive crystal to generate a high-power, diffraction-limited laser beam at 860 nm. Using a single flared amplifier, we obtain 1.09 W in a diffraction-limited beam from 2.2 W of pump power. Using an array of flared amplifiers, we also demonstrate efficient beam coupling, showing that this technique is easily extended to semiconductor amplifier arrays. © 1997 Optical Society of America

In this Letter we present a simple yet effective method for extracting a diffraction-limited light beam from the highly filamented output of flared semiconductor amplifiers and multi-amplifier arrays. Semiconductor flared amplifiers now routinely emit a few watts of light in a diffraction-limited beam when driven at currents of a few amps.<sup>1</sup> However, when driven at higher currents they develop a spatial instability that splits the output beam into a number of narrow filaments.<sup>2,3</sup> This filamentation, which is intrinsic to the laser diode gain medium, dramatically distorts both the amplitude and the phase of the amplified beam. The resulting distorted beam is far from diffraction limited and cannot be focused into a single-mode fiber, say, for telecommunication applications.

Using the technique demonstrated here, we can now operate laser amplifiers and amplifier arrays at high currents and still obtain a diffraction-limited output beam. We have eliminated problems caused by beam fanning in the photorefractive crystal and controlled the effects of heating by decreasing the crystal's absorption and by defocusing the pump beams and distributing them through the volume of the crystal.

The heart of our system is a photorefractive crystal that transfers energy from the high-power distorted beam of the amplifiers into a diffraction-limited signal beam.<sup>4-6</sup> The crystal acts as a real-time hologram to compensate actively for the wave-front distortions in the high-power laser amplifier.

This technique requires that the light from the laser amplifiers be coherent with the signal beam at the photorefractive crystal. Therefore we used a master-oscillator diode both to seed the semiconductor amplifier and to provide the signal beam to the crystal. Although the laser amplifier's output beam can be spatially distorted by nonlinearities in the gain medium, its spectrum remains identical to that of its injected signal, even at high operating currents.

In our initial experiments we used a single flared amplifier injected by a 500-mW tunable laser diode

(SDL 8630) with an  $\sim 5$ -mm coherence length. The output from the tunable laser was a diffraction-limited, collimated, circular Gaussian beam  $\sim 2$  mm in diameter. Figure 1 shows that this injecting beam passed through an optical isolator before a beam splitter divided the laser's output into signal and pump beams. We directed the signal beam exactly parallel to the 6.22-mm-long  $c$  axis of a Hughes-grown rhodium-doped  $\text{BaTiO}_3$  crystal (#BT315A1).<sup>7</sup> We focused the pump beam into a single, 3.1-mm-long semiconductor flared amplifier, first using a filter to attenuate the pump to 40 mW to avoid damaging the semiconductor amplifier's entrance face. With this injected light and at a current of 8 A the semiconductor amplifier generated 2.35 W of aberrated light. A spherical lens collected the aberrated output from the flared amplifier and directed its elliptical beam into an  $a$  face of the  $\text{Rh}:\text{BaTiO}_3$  crystal. We matched the height of the pump beam to the  $\sim 2$ -mm height of the signal beam, producing a 4-mm beam width in the horizontal direction. The external angle of incidence of the pump

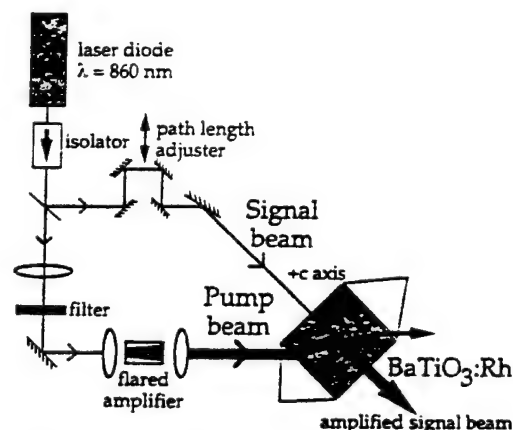


Fig. 1. High-power, photorefractive amplifier. The signal beam travels parallel to the crystal's  $c$ -axis direction and steals energy from the pump beam.

beam was  $45^\circ$ . We used a LaSFN9 coupling prism with a high refractive index ( $n = 1.83$ ) to generate an internal crossing angle of  $68^\circ$  between the pump and the signal beams inside the crystal. All beams were horizontally polarized. A path-length adjuster allowed us to match the signal and the pump paths to the crystal, ensuring that these two beams were mutually coherent inside the crystal. The photorefractive crystal transferred energy from the pump beam to the signal beam through two-wave mixing.

We first illuminated the crystal with 0.22 W of incident signal power and saw 0.125 W transmitted through the crystal. We then turned on a pump beam of 2.20 W and saw the transmitted signal power grow to 1.09 W; i.e., the crystal converted 44% of the pump beam into the diffraction-limited signal beam. If we had antireflection coated our crystal and optics to eliminate our sizable reflection losses, we believe that there would have been a transfer efficiency of 69% from the aberrated pump beam into the diffraction-limited signal beam.

The spatial quality of the amplified output beam was near the diffraction limit. In the vertical direction there was essentially no change in the profile of the signal beam as it was amplified in the crystal. Figure 2(a) shows that, in the horizontal direction, there was a slight change in the profile of the signal beam caused by depletion of the pump beam across the width of the signal beam. As an additional check on the spatial quality of the amplified signal beam, we focused it with an  $f = 500$  mm lens to obtain the spots shown in Figs. 2(b) and 2(c). We measured  $1/e^2$  spot radii of 138 and  $139 \mu\text{m}$  for the unamplified and the amplified signal beams, respectively. These values correspond to 1.01 and 1.04 times the diffraction limit, respectively, and demonstrate that photorefractive amplification maintains the spatial quality of the signal beam.

The above geometry does not necessarily yield the highest photorefractive two-beam coupling gain in  $\text{BaTiO}_3$ .<sup>6</sup> However, it does have two desirable features. First, a signal beam traveling exactly along the  $c$  axis is not noticeably depleted by beam fanning. Second, by making the signal and the pump beams cross at such a large internal angle, we ensure that spatial aberrations in the pump beam will be well averaged over the entire width (although not the height) of the signal beam.

To extract the maximum energy from the pump beam, we require a large two-wave-mixing gain coefficient  $\Gamma$  and a low absorption coefficient  $\alpha$ . However, these two parameters are not independent, and a partially reduced  $\text{Rh}:\text{BaTiO}_3$  crystal proved an ideal compromise. By carefully controlling the reduction conditions, we were able to lower significantly the absorption coefficient of our as-grown crystals while maintaining a relatively high effective photorefractive trap density. Decreasing the absorption also minimized heating of the crystal. The details of the reduction process are described elsewhere.<sup>9</sup> The crystal (#BT315A1) used in the above experiments at  $\lambda = 860$  nm had an absorption coefficient of  $\alpha = 0.35 \text{ cm}^{-1}$  and a photorefractive trap density of  $6 \times 10^{16} \text{ cm}^{-1}$

(measured with an absorption grating technique<sup>10</sup>). From the measured beam interaction length and the known trap density for this crystal, and using a three-dimensional depleted pump-amplification model, we calculate an effective gain coefficient of  $\Gamma = 8.6 \text{ cm}^{-1}$ .

To test the response of our system to an even more highly aberrated pump beam, we replaced the single flared amplifier with an array consisting of four flared amplifiers coupled to a single input port through a branched waveguide network.<sup>11</sup> We required a bigger crystal (BT#306A), which unfortunately also had a bigger absorption ( $\alpha = 0.85 \text{ cm}^{-1}$ ). We modified the beam collection optics as shown in Fig. 3. When injected with 40 mW from the master oscillator, this

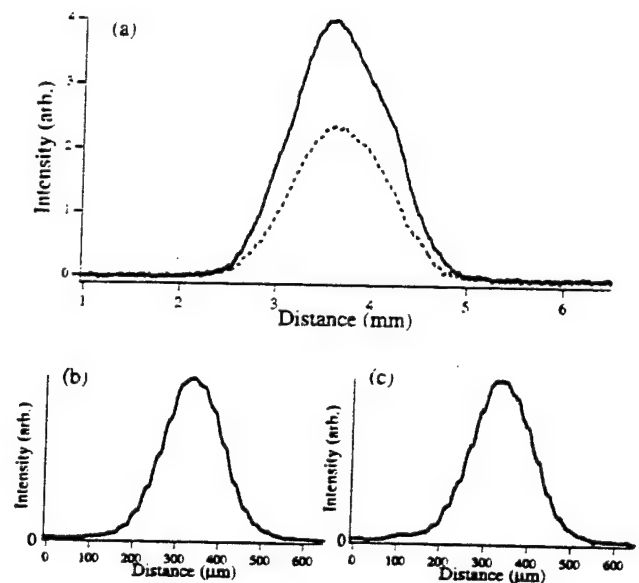


Fig. 2. Horizontal spatial profiles of the transmitted signal beam with and without amplification from the pump beam in the photorefractive crystal. A single flared semiconductor amplifier is the pump source. (a) Signal beam at exit face of the crystal without ( $\times 5$ ; dashed curve) and with (solid curve) the pump. (b) Signal beam at the focus of an  $f = 500$  mm lens without the pump. (c) Signal beam with the pump. The steps are caused by the individual pixels in our linear detector array. The vertical scales are different in (b) and (c). The pump beam is seen to amplify the signal beam without causing any measurable distortion.

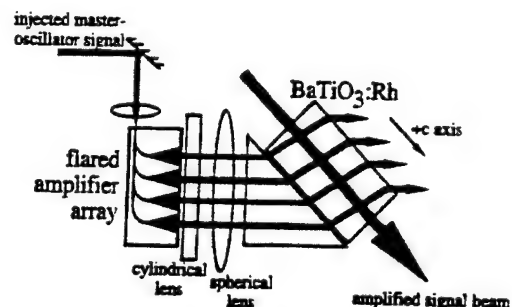


Fig. 3. Detail of the optical setup with an array of flared amplifiers now generating the pump beam.

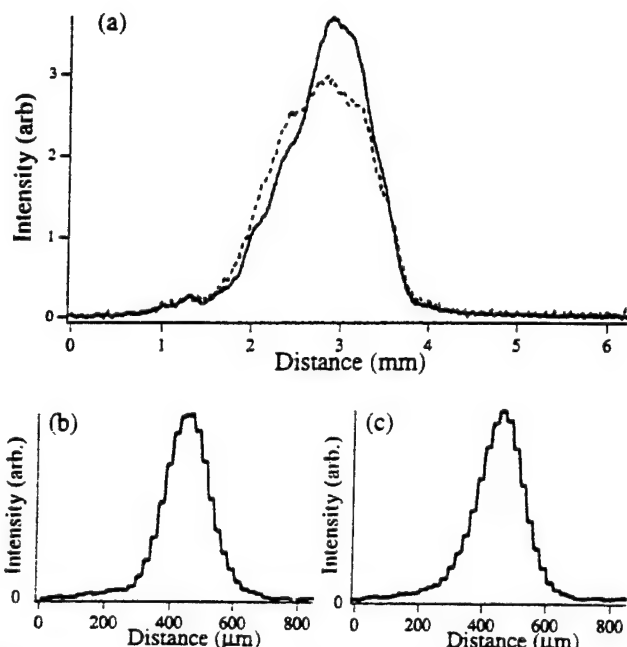


Fig. 4. Horizontal spatial profiles of the transmitted signal beam with and without amplification in the photorefractive crystal. An array of flared amplifiers is the pump source. (a) Signal beam at exit face of crystal without ( $\times 10$ ; dashed curve) and with (solid curve) the pump. (b) Signal beam at the focus of an  $f = 500$  mm lens without the pump. (c) Signal beam with the pump. The steps are caused by the individual pixels in our linear detector array. The vertical scales are different in (b) and (c).

amplifier array produced a coherent output power of 1.8 W at a current of 7 A. With this 1.8 W of pump power and 0.12 W of signal power incident upon the crystal, we obtained an amplified output beam of 0.26 W. The disappointingly small value of the output power was caused primarily by the too-large absorption coefficient of the BaTiO<sub>3</sub> crystal used.

Figure 4(a) shows the transmitted signal beam profile with and without the pump beam present. Even with this pump array operating in the strongly depleted pump regime, we observed good fidelity in the amplified signal beam. As before, we checked the spatial phase front of the amplified signal beam by focusing it with an  $f = 500$  mm lens to obtain the profile shown in Figs. 4(b) and 4(c). Here the  $1/e^2$  radii of both the unamplified and the amplified signal beams corresponded to 1.1 times the diffraction limit, implying that the photorefractive amplifier had caused no additional aberration. Using the flared amplifier array, we measured an effective beam coupling coefficient of  $\Gamma = 4.2 \text{ cm}^{-1}$  in the same coupling geometry and crystal as above. However, for this configuration we calculate a two-beam coupling coefficient of  $5.5 \text{ cm}^{-1}$ . We attribute this difference to the presence of increased amplified spontaneous emission noise in some elements of the flared amplifier array. This incoherent optical noise acts as an erasing beam to erase partially the photorefractive gratings and decrease the photorefractive gain. We found that blocking the output from one element of the flared amplifier array reduced its total output power from 1.8 to 1.1 W but

produced essentially no change in the amplified beam power. This suggests that light from this array element was only weakly coherent with the master oscillator and was more of a hindrance than a help.

In summary, we have demonstrated the feasibility of using two-wave mixing in a photorefractive crystal to clean up the aberrated wave front of a high-power (2-W) semiconductor laser. The final output beam is essentially diffraction limited. Pump-signal transfer efficiencies of 44% have been demonstrated, with 69% achievable by simply antireflection coating the crystal faces. The system can clean up the wave front of either a single-laser pump source or an array of temporally coherent sources. Recently an eight-element array of flared amplifiers generated an output of 40 W (pulsed) of spectrally coherent light, demonstrating that high powers are attainable from such coherent semiconductor sources.<sup>12</sup> With such incident pump power, a moderate crystal absorption, and heat sinking the crystal at a single surface, we calculate a maximum crystal temperature increase of less than 20°C, which is tolerable. With proper thermal design, the temporally coherent output from such a high-power amplifier could be channeled into a single, diffraction-limited beam by use of the above techniques.

This research was funded by the U.S. Air Force Phillips Laboratory, Kirtland Air Force Base, New Mexico.

## References

1. S. O'Brien, D. F. Welch, R. A. Parke, D. Mehuys, K. Dzurko, R. J. Lang, R. Waarts, and D. Scrifres, *IEEE J. Quantum Electron.* **29**, 2052 (1993).
2. R. J. Lang, A. Hardy, R. Parke, D. Mehuys, S. O'Brien, J. Major, and D. Welch, *IEEE J. Quantum Electron.* **29**, 2044 (1993).
3. L. Goldberg, D. Mehuys, M. R. Surette, and D. C. Hall, *IEEE J. Quantum Electron.* **29**, 2028 (1993).
4. S. MacCormack and R. W. Eason, *Opt. Lett.* **15**, 1212 (1990).
5. W. R. Christian, P. W. Beckwith, and I. McMichael, *Opt. Lett.* **14**, 81 (1984).
6. J. M. Verdiell, H. Rajbendach, and J. P. Huignard, *IEEE Photon. Technol. Lett.* **2**, 568 (1990).
7. B. A. Wechsler, M. B. Klein, C. C. Nelson, and R. N. Schwartz, *Opt. Lett.* **19**, 536 (1994).
8. Y. Fainman, E. Klancnik, and S. H. Lee, *Opt. Eng.* **25**, 228 (1983).
9. B. A. Wechsler, G. D. Bacher, C. C. Nelson, M. B. Klein, S. MacCormack, and J. Feinberg, in *Nonlinear Optics: Materials, Fundamentals, and Applications*, Vol. 11 of 1996 OSA Technical Digest Series (Optical Society of America, Washington D.C., 1996), paper NTuA4.
10. R. M. Pierce, R. S. Cudney, G. D. Bacher, and J. Feinberg, *Opt. Lett.* **15**, 414 (1990).
11. J. S. Osinski, D. Mehuys, D. F. Welch, R. G. Waarts, J. S. Major, Jr., K. M. Dzurko, and R. J. Lang, *Appl. Phys. Lett.* **66**, 556 (1995).
12. J. S. Osinski, D. Mehuys, D. F. Welch, K. M. Dzurko, and R. J. Lang, *IEEE Photon. Technol. Lett.* **6**, 1185 (1994).

# Ballistic-Light Imaging with Temporal Holography: Using Causality to See through a Scattering Medium<sup>a</sup>

JACK FEINBERG<sup>b,c</sup> AND ALEX REBANE<sup>d</sup>

<sup>c</sup>*Department of Physics  
University of Southern California  
Los Angeles, California 90089-0484*

<sup>d</sup>*Physical Chemistry Laboratory  
ETH-Zentrum, CH-8092  
Zurich, Switzerland*

## INTRODUCTION

Here I review the remarkable properties of temporal holography. Ordinary holography recreates a still image, while temporal holography recreates images in time, like the frames in a movie. The images can be picoseconds apart. If the early images show light that has passed through a scattering medium without scattering, then by selectively recreating these early images one can reveal a structure hidden inside the material. Although temporal holography is attractive for medical imaging, it has limitations. In this paper we show how the principle of causality lies at the heart of temporal holography. A brief experimental account of this experimental work is found in Reference 1, which we adapt here to form the first part of this paper. A more detailed mathematical treatment can be found in Reference 2.

In a conventional hologram one records the interference pattern of two light beams arriving at the same time on a light-sensitive material, such as photographic film. In contrast, in temporal holography a molecular resonance is used to record an interference pattern between light signals that arrive at different times. This technique creates a hologram with temporal resolution. Using a timed reference pulse as a "light shutter," we can record holographic images selectively, according to the time taken by light traveling from the object to the hologram. We use this method to image an object behind a semiopaque screen, and indicate how a similar method could be used to inspect objects embedded in a dense scattering medium. In principle, such a technique might be applied to the medical imaging of tumors. (In practice, the small ratio of signal-to-noise of this technique limits its applicability to imaging through thin tissue.)

<sup>a</sup>One of the authors (J.F.) gratefully acknowledges support from the U.S. Air Force Office of Scientific Research.

<sup>b</sup>Corresponding author. Phone: (213) 740-1134; fax: (213) 740-6653; e-mail: feinberg@physics.usc.edu



### PIANOS WITH STRINGS

Consider a piano with its dampers removed, so that its strings are free to vibrate. Kicking the piano will excite all of its strings. However, singing loudly near this piano will excite only some of its strings, namely those strings in resonance with notes in the music. Consider the following experiment. First sing a song to the piano, such as: "A pretty face is like a melody. . . ." Then, after a delay time,  $T_0$ , short compared to the damping time of the strings, kick the piano once. Some of the strings will now be ringing wildly, while others will be barely moving. In particular, those strings that were excited by the singing but are vibrating out of phase with the kick will have their energy diminished by the kick. Now, modify the coupling of each string according to the energy it has after the kick. (For example, cut the strings that are barely moving, so that they can move no more.) In a brief and little known paper, H. C. Longuet-Higgins<sup>3</sup> showed that if one now kicks the piano again, then after that same delay time,  $T_0$ , a replica of the original melody will be played by the piano's remaining strings! Even more interesting, if the first kick occurred in the middle of a phrase, then only the later parts of the phrase will emerge after the second kick. For example, if the piano is prepared by "A pretty face (*kick!*) is like a melody. . . ." then, after its strings are modified as just described, a second kick to the piano will bring forth, " . . . is like a melody. . . ." The kicked piano forms a "temporal shutter" that replays only the musical wave that arrived after the first kick.

### PIANOS WITH MOLECULES

In this work we create a type of "optical piano" that stores and later recreates the early or the late parts of an optical wave. The 88 narrow-frequency resonators of an ordinary acoustic piano are here replaced by 20,000 narrow-frequency resonators of a hole-burning material. We create this bank of narrow-frequency resonators by doping the organic dye protoporphyrin into a solid block of polystyrene.<sup>2,4-7</sup> Each dye molecule acts as a lightly damped resonator, but due to inhomogeneities in the plastic matrix, each dye molecule has a slightly different resonant frequency. Cooling the polystyrene to 2 K makes the phase-relaxation time of the molecule's upper level become quite long ( $T_2 \approx 1$  ns), so that each absorption has a narrow homogeneous spectral width of  $\Delta\omega = 1/(\pi c T_2) \approx 0.01$  cm<sup>-1</sup>. The polystyrene matrix causes the net absorption spectrum of all of the molecules to form an inhomogeneously broadened band extending over a 200-cm<sup>-1</sup>-wide range. Consequently, this material resembles a bank of  $200/0.01 = 20,000$  narrow resonators.

We use this doped plastic to record and store the spectral and spatial contents of an incident light beam. When illuminated by narrow-band light of frequency  $\omega$ , those molecules that happen to be in resonance with the light become excited. A fraction of these excited molecules subsequently relaxes

into a metastable state (which is thought to be a tautomerization of the original molecule). Once in this transformed state the molecule's absorption is shifted to a completely different spectral region, so a narrow "hole" is burned into the sample's absorption spectrum at the frequency  $\omega$ . This spectral hole remains as long as the sample is kept cold.

### EARLY VS. LATE

Consider two optical pulses incident on a holographic recording medium as shown in the inset of FIGURE 1. Let pulse F arrive  $T_0$  seconds before pulse G. If we were to use photographic film as the recording medium, then an interference pattern will be recorded only if the pulses overlap with each other at least partially in time. But suppose we replace the photographic film by a bank of resonators in a spectral hole-burning material, as described earlier, with each resonator atom tuned to a slightly different optical frequency  $\omega_j$ . In this case the interference pattern of the two optical pulses F and G can be recorded even if the pulses are never present in the material at the same time.<sup>3</sup>

If the optical pulse F is sufficiently brief, then its frequency spread will be sufficiently wide to excite all of the atoms, much like a brief kick to a piano will excite all of the piano's strings. Each atom will continue to ring at its own natural frequency  $\omega_j$ . After a delay time  $T_0$  the second light pulse G arrives, and it will transfer energy either into or out of the  $j$ th atom *depending on the relative phase* between G's optical electric field and the phase  $\phi_j = \omega_j T_0$  of the still-ringing atom. Because each atom's phase depends on its own particular resonant frequency  $\omega_j$ , a given time delay  $T_0$  between the two incident light pulses will produce a unique pattern of excited and unexcited atoms in frequency space.

After interacting with both of the light pulses F and G, let the absorption of the  $j$ th atom be permanently altered by an amount proportional to the atom's final energy (much like we altered the piano's strings in the preceding example). In particular, if the material consists of a hole-burning medium, then those molecules that were excited after both pulses become removed from the absorption spectra; they leave an absorption hole behind. If the bank of now-altered resonators is illuminated by a replica of the brief pulse F, it will absorb and reradiate light, again at the frequencies  $\omega_j$  appropriate to each atom. At first, the phases of the reradiated light will be incoherent, but after a time of exactly  $T_0$ , the phases of the different frequencies come together to reproduce coherently a duplicate of the pulse G.<sup>3</sup> It can be shown,<sup>2</sup> however, that application of a replica of pulse G to the altered atoms causes a reradiation of light that loses rather than gains phase coherence with the passage of time. Unlike conventional off-axis holography, where either light beam can be used to reconstruct the other, the bank of atoms here records the direction of time's arrow.

Now consider illuminating an entire scene with a pulsed laser. Record the

reflected light  $G$  using a bank of tuned resonators, and let a reference pulse  $F$  also illuminate the resonators, as described before. If the reference pulse arrives at the resonators *before* any of the reflected light, then the entire scene can be recalled by simply reading with another reference pulse. However, if the initial reference pulse is delayed so that it arrives *after* some of the reflected light, then reading (with another reference pulse) will only recreate those parts of the image that arrived after that first reference pulse, that is, those parts of the scene that were located farthest from the resonators. For

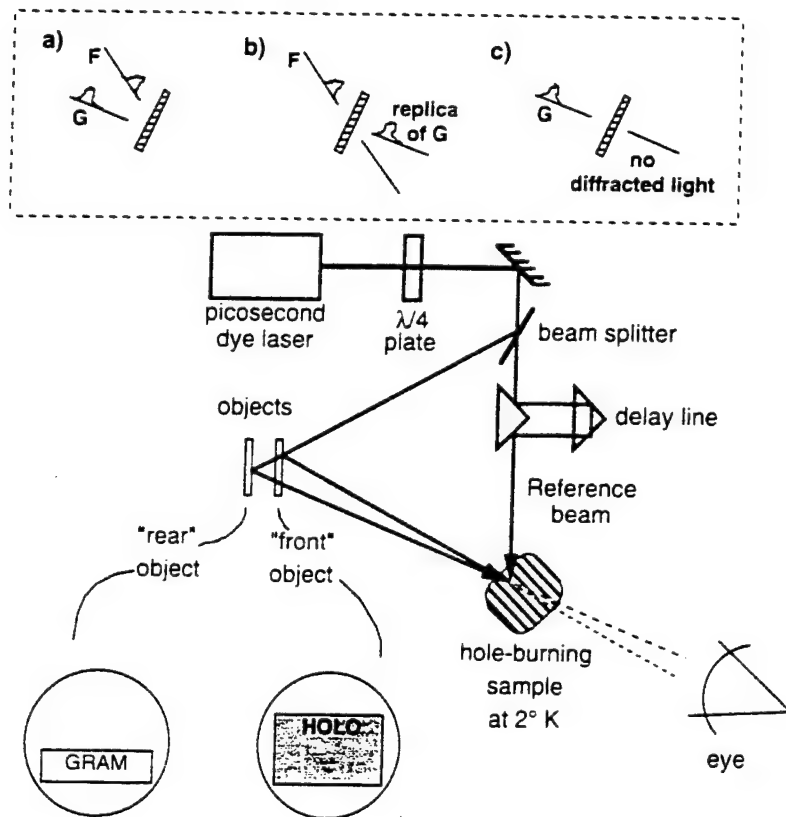


**FIGURE 1. (Inset)** (a) Writing the spectral hole-burning hologram with two light pulses separated in time. (b) Reading with the earlier pulse  $F$  recreates the later pulse  $G$ . (c) Reading with the later pulse  $G$  does not produce any diffracted pulse. **(Lower portion)** Experimental setup. The front object is a frosted slide with the letters "HOLO" pasted on the front. The rear object is the letters "GRAM" pasted on the back of the same slide.

example, if the scene consisted of the street view of a bookstore, then, with a suitably timed reference pulse, the reconstructed image would show the books on display deep inside the store, and would not show the reflections off of the bookstore's nearby front window.

It is also possible to reproduce the early light rather than the late light, that is, the light that strikes the hologram *before* the reference pulse arrives. To produce such an image, the hologram is read out by a replica of pulse  $F$  applied in the opposite direction to the original pulses: reversing the spatial orientation of the readout pulse reverses the relative phase relation of the

reradiated light, and thereby leads to the recreation of the "early" rather than the "late" scattered light.

### AN EXPERIMENTAL DEMONSTRATION

In our experiments the hole-burning medium was a 3-mm-thick block of polystyrene doped with protoporphyrin at a concentration of  $10^{-3}$  mole/L. The useful sample area was 4 cm<sup>2</sup>. The sample was immersed in liquid helium, and the helium vapors were pumped to reduce the temperature to 2 K. The peak of the broad absorption feature was at  $\lambda = 621$  nm, at which the optical density was 1.6. The light source was a continuous-wave model-locked Nd:YAG laser (Coherent Antares 76 s) that synchronously pumped a tunable dye laser (Coherent 701) to produce pulses having an intensity temporal width of 8 ps full-width at half-maximum (FWHM). (These pulses were not transform limited; they had a coherence length of only 0.5 ps). The repetition rate of the laser pulses was 76 MHz. A beamsplitter divided the beam from the picosecond dye laser into a reference beam and a separate beam to illuminate the various objects in the scene, as shown in FIGURE 1. The reference beam was expanded by a telescope to fully illuminate the polystyrene block. Scattered light from the illuminated objects simply propagated to the polystyrene block with no intervening lens. The angle between the reference beam and the image-bearing beam was about 14°.

The recorded scene consisted of two objects. The nearby object was a 1.0-mm-thick glass slide with the letters HOLO attached to its front surface. The distant object was a white paper screen carrying the letters GRAM, which was pressed against the back of the transparent slide, so the separation between the two objects was about 1 mm. In order to increase the amount of light scattered by the slide, its front surface was sprayed with white Christmas tree flocking. The slide was then illuminated from the front. Of the scattered light from the slide reaching the polystyrene block, about 80% came from the front sprayed surface of the slide, and only 20% came from the rear surface. Viewing the laser-illuminated slide by eye from the position of the polystyrene block, one could clearly read the words HOLO, but the intense glare from the front surface almost completely obscured the letters GRAM located near the back of the slide. (This is in analogy with the glare caused by the bookseller's glass window obscuring the titles of the books located behind the window.)

Light from the laser reached the front of the slide 5 ps before it reached the back of the slide. Consequently, light from the front of the slide reached the storage medium 10 ps (twice the glass travel-through time) before light from the back of the slide. In the first experiment a hologram was recorded with the reference beam timed to arrive before both of these object waves. In the second experiment a hologram was recorded with the reference beam carefully timed to arrive within the 10 ps interval between the two object waves.

The reference beam and the object beam each had an average intensity of

0.2 mW/cm<sup>2</sup> at the location of the storage medium. An exposure time of 2–3 min was needed to record a hologram with a fluence of 70–100 mJ/cm<sup>2</sup>, corresponding to 10<sup>10</sup> identical pairs of laser pulses. To write the first hologram we tuned the laser wavelength to the absorption maximum of the medium at 621 nm. Because the absorption spectrum is 200 cm<sup>-1</sup> wide while the dye-laser pulses have a spectral bandwidth of only ~30 cm<sup>-1</sup>, we could change the wavelength of the dye laser by some 30 cm<sup>-1</sup> and then record a new hologram in a fresh spectral region of the storage medium without affecting any previously stored holograms. The different holograms written at different center wavelengths were later selectively read out by simply adjusting the center wavelength of the reading dye-laser pulse. In the absence of all illumination these holograms lasted for as long as the sample was kept cold, months if desired (although liquid helium is expensive).

Readout of the holograms was performed by blocking the light coming from the objects and illuminating the hologram with only the reference beam. FIGURE 2a shows the reconstructed image when the hologram was recorded using a reference beam that arrived a few picoseconds before any of the light from the glass slide. The letters HOLO on the front of the slide are plainly visible, but the glare from the front of the slide all but obscures the letters GRAM located near the back of the slide. FIGURE 2b shows the reconstructed image when the reference beam pulse was carefully set to arrive after light from the distant object but before light from the nearby object. Now only the distant object is reconstructed, and the nearby object is eliminated. We emphasize that the light from these objects need not arrive at the polystyrene block at the same time as light in the reference pulse in order for the hologram to be recorded. In fact, because the coherence time of the light pulses was only 0.5 ps, and because we set the reference beam to arrive at the storage medium about 5 ps before the light from the back of the slide, the reference and object beams could not have produced a conventional intensity interference pattern in the storage medium. We note that the maximum time delay permitted between the object and reference beams was 10<sup>3</sup> ps and is set by the phase-decay time  $T_2$  of the sample.

In the experiment reported here we were able to selectively reconstruct those objects that sent light to the hologram *after* the reference pulse had arrived, that is, the "late" light. However, for some applications it is desirable to do the opposite and recreate the light that arrived *before* the reference pulse, that is, the "early" light. For example, consider the problem of imaging an object that is embedded in a scattering medium, such as a tumor embedded in breast tissue. Illuminate the tissue from behind with a short laser pulse. Light transmitted through the tissue without any scattering will emerge before light that has been multiply scattered by the tissue.<sup>8</sup> Because the eye records all of this light, and because the scattered light overwhelms the unscattered light, the tumor remains unseen. However, if light that arrived earlier at the eye could be selectively enhanced, then a shadowgram of the tumor would become visible.



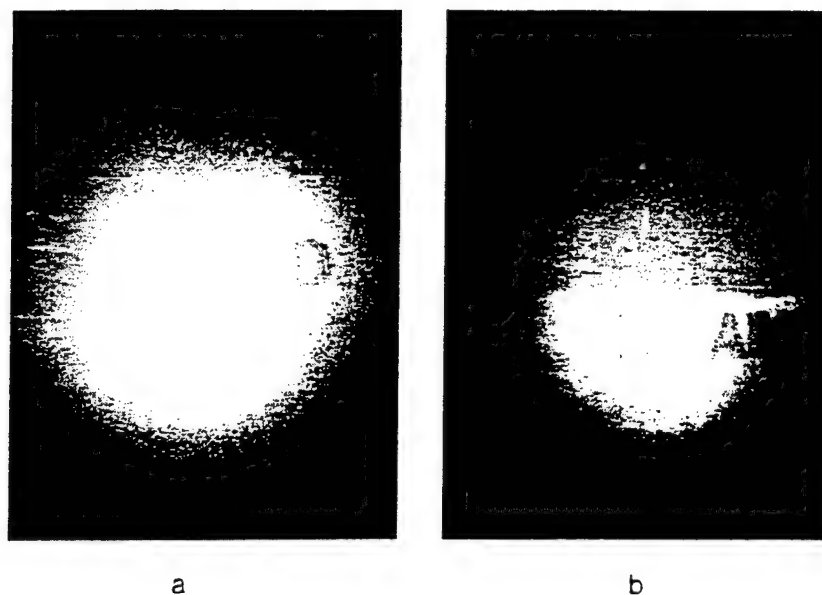


**FIGURE 2.** (a) Holographic reconstruction of both objects. The reference pulse was set to arrive before light from either of the objects. The glare from the frosted glass in front with the word HOLO obscures the object GRAM behind it. (b) In this hologram the reference pulse was delayed to arrive after light from the front object (frosted glass) but before light from the rear object. The front object is no longer reconstructed, while the rear object (GRAM) is now plainly visible.

This selection of early light over late light can be accomplished by simply altering the direction of the readout beam used in the preceding experiments. Instead of using a readout beam that is in the same direction as the reference beam, one should use a readout beam that is directed exactly opposite to the direction of the original reference beam. This is the "four-wave mixing" geometry of traditional phase-conjugation experiments,<sup>9</sup> but with a spectral hole burning material, now only the light that arrived before the reference beam is holographically reconstructed in the final image. In this way light scattered from back-lighted tissue could be eliminated, while light traveling directly through the tissue could be preserved, and would form a shadowgram of features embedded in the tissue.

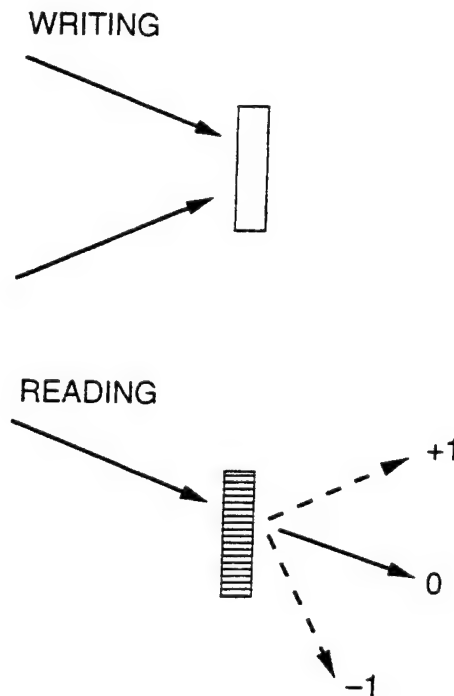
Recently we achieved real-time imaging by using a different hole-burning material to speed up our writing time from 120 s to a few tens of milliseconds (personal communication). We use Zn-tetrabenzoporphin in a polymer film. This molecule does not show any permanent holes as in our previous samples, but has transient holes with a lifetime of 50 ms. Excited molecules can end up shelved in the triplet ground state for about 50 ms before they decay down to the singlet ground state. There are two advantages to this type of material. First, we can write a new hologram every 50 ms because the old one goes away. Second, the yield of the transition to the triplet state is at least ten times better than the yield of the tautomerization reaction in our previous sample. By using a bit more laser power than before we were able to write a hologram

in a few tens of milliseconds, and, with the help of two mechanical shutters, we could write and then view holograms in real time. A particularly nice image was that of a wristwatch, where the seconds indicator of the reconstructed image could be clearly seen to move with time.

### WHY DOES IT WORK?

Why does temporal holography work? How can the early or the late portions of a light wave be preferentially selected from a hole-burning hologram? The explanation resides with the principle of causality. A key fact is that if one writes a simple plane-wave grating in a hole-burning material using short pulses, then that grating will deflect light only in one direction (say the  $+k$ -direction, where  $k$  is the grating's wavevector) and not in the other direction (i.e., the  $-k$ -direction).

Consider a thin-phase hologram formed, not in a hole-burning material, but by two plane waves interfering in a thin piece of photographic film. As shown in FIGURE 3, when this thin, conventional hologram is read by either of the writing beams, both the  $+1$  and the  $-1$  diffraction orders appear, because the spatially periodic deformation of the film has the form  $\cos(kx)$ , which



...both  $+1$  and  $-1$  diffracted orders appear.

**FIGURE 3.** Two plane waves interfere in a photographic film to make a conventional thin hologram. Reading with either wave reconstructs both the  $+1$  and the  $-1$  diffraction orders.

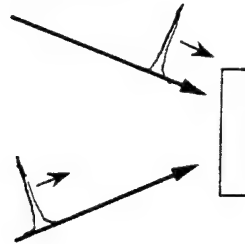
contains both  $+k$  and  $-k$  terms:

$$\cos(kx) = 1/2 [\exp(+ikx) + \exp(-ikx)].$$

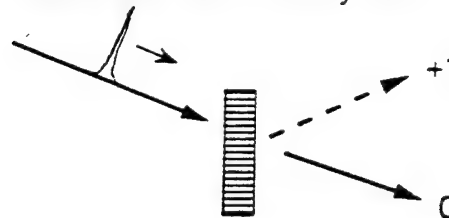
Next consider a hologram created in a thin, hole-burning material by two light pulses incident from the same side and that do not overlap in time, as shown in FIGURE 4. Now only the  $+1$  diffracted order appears when either of the writing beams is used to read the hologram; the  $-1$  order is mysteriously absent.

If we use thick instead of thin holograms, then the Bragg condition must also be obeyed, as shown in FIGURES 5 and 6. In the thick, ordinary hologram either reading beam yields a diffracted beam, but in the thick, hole-burning material only the early writing beam yields a diffracted beam. Reading with the late beam yields no diffracted light at all, because the  $+k$  grating violates the Bragg condition, and in the thick, hole-burning hologram the  $-k$  grating is

#### WRITING



#### READING from the early side:



#### READING from the late side:

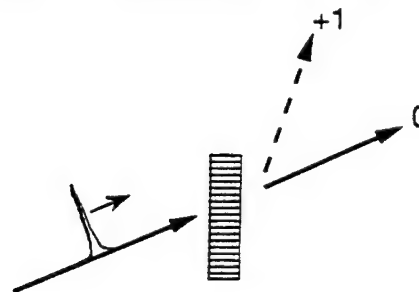
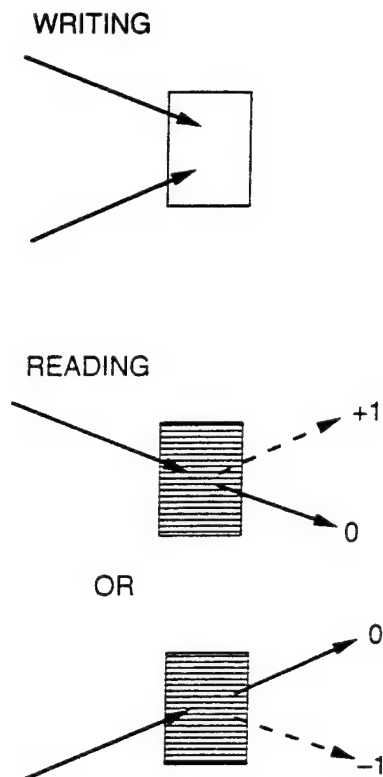


**FIGURE 4.** Two short pulses impinge on a thin, hole-burning medium. Reading with either of the writing beams produces only the  $+1$  diffraction order.



...the Bragg condition for a thick hologram  
permits only one diffraction order

FIGURE 5. A thick ordinary hologram yields diffracted light for either reading beam.

apparently absent when read with a beam incident from the same side as the writing beams.

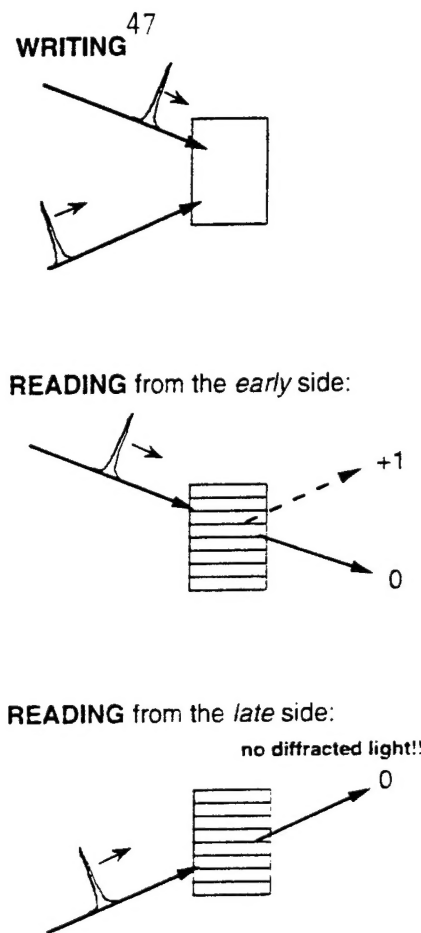
The reason that only the  $+k$  order appears in a hole-burning medium using the geometry of FIGURES 4 and 6 is hidden in the mathematics of causality. Let the holographic material, whatever it may be, have a temporal response given by  $r(x, t'')$  at position  $x$  and time  $t''$  from an excitation at time  $t'$ . If the response function does not change from day to day, then it is a function only of the difference  $t \equiv t'' - t'$ . Causality then demands that the response function bow to the following wonderfully powerful constraint:

$$r(x, t) = r(x, t) * h(t), \quad (1)$$

where  $h(t)$  is the Heaviside step function, defined as

$$h(t) \equiv 0 \quad \text{for } t < 0; \quad h(t) \equiv 1 \quad \text{for } t \geq 0.$$

Equation 1 says that there is no response *before* the impulse (i.e., you can't win the lottery if you don't buy a ticket). In the frequency domain this



...reading from the late side gives no diffracted light for a thick, hole-burning hologram.

**FIGURE 6.** A thick, hole-burning hologram yields diffracted light only if read from the "early" side.

causality constraint becomes (with a bit of math)

$$R(x, \omega) = \frac{1}{\pi} \left( \frac{1}{i\omega} \otimes R(x, \omega) \right). \quad (2)$$

where the symbol  $\otimes$  denotes convolution. (This convolution leads to the familiar coupling between the real and imaginary parts of the material's response function in the frequency domain, and gives the Kramers-Kronig relations, etc.)

Now, consider the following simple arrangement: two writing beams impinge on a hole-burning material from the same side, with a delay  $\tau$  in one beam as shown in FIGURE 7. These light beams will create a spatially periodic grating in the material's absorption (i.e., a spatially periodic "hole") that has a different phase different for each optical frequency  $\omega$ :

$$R(x, \omega)_{\text{imag}} = R_0 \cos(k \cdot x + \omega\tau). \quad (3)$$



Note that each frequency has its own phase delay  $\omega\tau$ . This is the key fact. One cannot write such gratings in photographic film or in a photorefractive crystal such as barium titanate, because in those materials all nearby reading frequencies  $\omega$  see the *same* grating. But by using a hole-burning material, one can "burn in" different absorption gratings at different, closely spaced optical frequencies  $\omega$ , with each grating having a different phase  $\phi = \omega\tau$ . Note that by inserting a fixed time delay  $\tau$  in one of the two writing beams, one creates precisely the  $R_{\text{imag}}$  given in Eq. (3). Then causality in the form of Eq. (2) dictates that  $R_{\text{real}}$  must be of the form:

$$R(x, \omega)_{\text{real}} = -R_0 \sin(k \cdot x + \omega\tau), \quad (4)$$

and combining Eqs. (3) and (4) gives:

$$\begin{aligned} R(x, \omega) &= R(x, \omega)_{\text{real}} + iR(x, \omega)_{\text{imag}} \\ &= iR_0[\cos(kx + \omega\tau) + i \sin(kx + \omega\tau)] \\ &= iR_0 \exp[+ikx] \exp[+i\omega\tau], \end{aligned} \quad (5)$$

which is the desired result, namely, that when reading with one of the writing beams, only the  $\exp[+ikx]$  grating is present and not the  $\exp[-ikx]$  grating.

### THE +K GRATING SLICES TIME

To see why the presence of only the  $+k$  grating allows one to preferentially select either the early or the late parts of a stream of light, consider FIGURE 8. Here a light stream and a short "marker" reference pulse expose a thick, hole-burning material. Reading the resulting hologram with a duplicate of the marker pulse itself recreates only those parts of the light stream that arrived *after* the marker pulse. That is because the early parts of the light

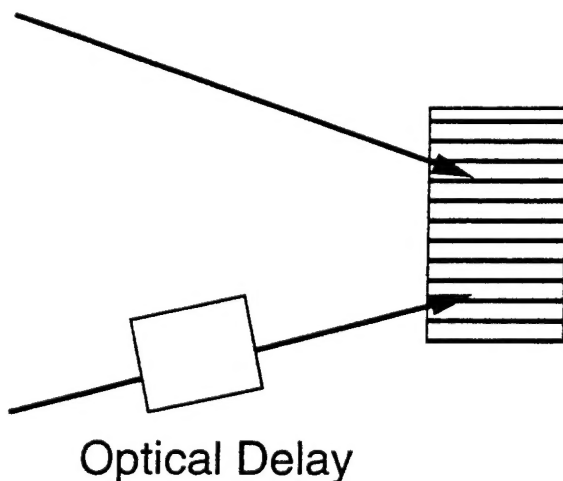
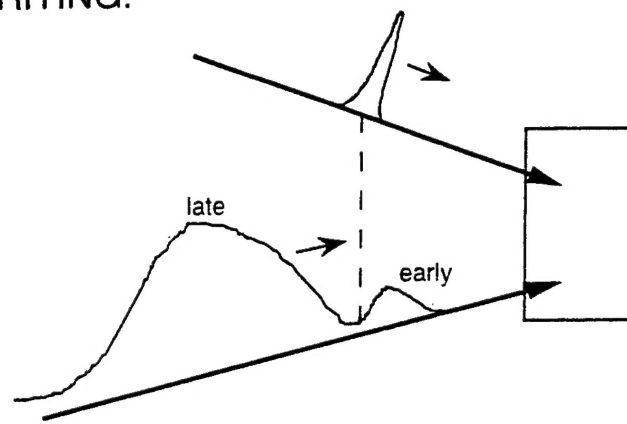


FIGURE 7. Inserting an optical delay  $\tau$  in the path of one beam creates different holograms for different frequencies in a hole-burning material.

WRITING:

49



READING:

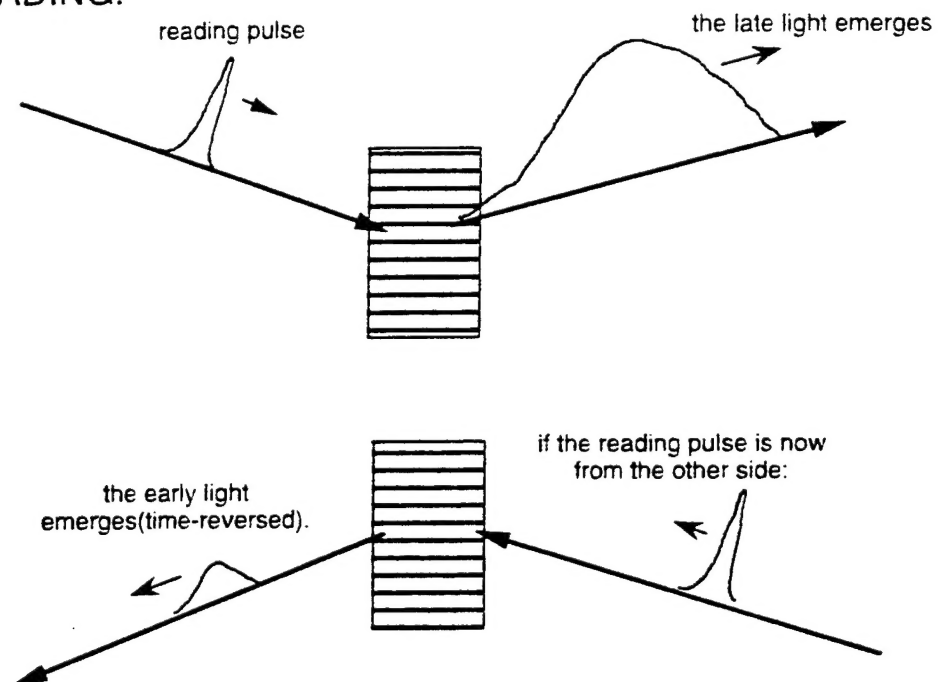


**FIGURE 8.** Expose a hole-burning material with a stream of light and also a short reference pulse. Reading with a duplicate of the reference pulse yields the late light. Reading with the phase-conjugate replica of the reference pulse yields the early light.

stream would make the marker pulse be reading from the late side, and that gives no diffraction according to our discussion thus far, and as seen in the bottom of FIGURE 6.

This preferential recall of late light over early light is what we demonstrated in the photographs in FIGURE 2. However, to see through a scattering material, one wants the opposite, that is, the preferential display of the early,

ballistic light over the later scattered light, and for this one merely reverses the direction of the reading pulse to the phase-conjugate direction, as seen in the bottom of FIGURE 8.

We caution that for medical applications this imaging scheme requires a very large dynamic range for the hologram, because in thick tissue the scattered light can be much more intense than the unscattered light. We estimate that our present spectral hole-burning medium has a dynamic range limited to  $\sim 10^3$ , and so, by itself, is not particularly useful for imaging through thick tissue. However, it might prove useful for imaging through thin tissue or in conjunction with other optical shutters to improve the overall signal-to-noise ratio.

### SUMMARY

It is possible to record a temporal movie of the light emerging from a scattering medium. Later, the movie can replay either the first-arriving or the last-arriving photons with picosecond temporal resolution. This temporal movie is created by directing two light beams at a hole-burning medium made from a chunk of dye-doped plastic. One light beam comes from the scattering material, while the other light beam is usually a short pump pulse. In contrast to conventional holography, here the two light beams do *not* overlap in time at the hole-burning plastic. The exposed plastic records the arrival time of *all* of the light from the scattering medium, and will store this temporal movie for months, if desired. Later one can preferentially view the early parts of the movie, and thereby see only the ballistic photons, that is, those photons that were not appreciably deflected in their passage through the scattering medium. Shining the phase-conjugate replica of the original pump pulse on the plastic medium recalls the early parts of the original scene, but not the later parts. In effect the hole-burning material creates a temporal shutter that passes the early light but blocks the later light. We presented experimental results and explained, using the principle of causality, how the plastic hole-burning medium creates this temporal shutter.

### REFERENCES

1. REBANE, A. & J. FEINBERG. 1991. *Nature* **351**: 378-380.
2. SAARI, P., R. KAARLI & A. REBANE. 1986. *J. Opt. Soc. Am.* **B3**: 527-533.
3. LONGUET-HIGGINS, H. C. 1968. *Nature* **217**: 104.
4. MOSSBERG, T. W. 1982. *Opt. Lett.* **7**: 77-79.
5. REBANE, A., R. KAARLI, P. SAARI, A. ANIJALG & K. TIMPMANN. 1983. *Opt. Commun.* **47**: 173-176.
6. REBANE, A. 1988. *Opt. Commun.* **65**: 175-178.
7. MOERNER, W. E. 1988. *Persistent Spectral Hole Burning: Science and Applications*. Springer-Verlag, Berlin.
8. YOO, K. M. & R. R. ALFANO. 1990. *Opt. Lett.* **15**: 320-322.
9. HELLWARTH, R. W. 1977. *J. Opt. Soc. Am.* **67**: 1-3.